



AFRL-RY-WP-TR-2016-0070

TQUID MAGNETOMETER AND ARTIFICIAL NEURAL CIRCUITRY BASED ON A TOPOLOGICAL KONDO INSULATOR

Jing Xia, Zach Fisk, and Victor Galitski

University of California Irvine

MAY 2016
Final Report

Approved for public release; distribution unlimited.

See additional restrictions described on inside pages

STINFO COPY

**AIR FORCE RESEARCH LABORATORY
SENSORS DIRECTORATE
WRIGHT-PATTERSON AIR FORCE BASE, OH 45433-7320
AIR FORCE MATERIEL COMMAND
UNITED STATES AIR FORCE**

NOTICE AND SIGNATURE PAGE

Using Government drawings, specifications, or other data included in this document for any purpose other than Government procurement does not in any way obligate the U.S. Government. The fact that the Government formulated or supplied the drawings, specifications, or other data does not license the holder or any other person or corporation; or convey any rights or permission to manufacture, use, or sell any patented invention that may relate to them.

This report is the result of contracted fundamental research deemed exempt from public affairs security and policy review in accordance with SAF/AQR memorandum dated 10 Dec 08 and AFRL/CA policy clarification memorandum dated 16 Jan 09. This report is available to the general public, including foreign nationals.

AFRL-RY-WP-TR-2016-0070 HAS BEEN REVIEWED AND IS APPROVED FOR PUBLICATION IN ACCORDANCE WITH ASSIGNED DISTRIBUTION STATEMENT.

PACER.MARK
.J.1230148828

Digitally signed by
PACER.MARK.J.1230148828
DN: c=US, o=U.S. Government, ou=DoD,
ou=PKI, ou=USAF,
cn=PACER.MARK.J.1230148828
Date: 2016.04.25 12:53:05 -04'00'

MARK J. PACER
Program Manager
Devices for Sensing Branch
Aerospace Components & Subsystems Division

DETTMER.ROS
S.W.1076451806

Digitally signed by
DETTMER.ROSS.W.1076451806
DN: c=US, o=U.S. Government, ou=DoD,
ou=PKI, ou=USAF,
cn=DETTMER.ROSS.W.1076451806
Date: 2016.05.09 10:54:34 -04'00'

ROSS W. DETTMER
Chief
Devices for Sensing Branch
Aerospace Components & Subsystems Division

BEARD.TODD
W.1140628677

Digitally signed by BEARD.TODD.W.1140628677
DN: c=US, o=U.S. Government, ou=DoD, ou=PKI,
ou=USAF, cn=BEARD.TODD.W.1140628677
Date: 2016.05.18 10:01:19 -04'00'

TODD W. BEARD, USAF, Lt Col
Deputy Chief
Aerospace Components & Subsystems Division
Sensors Directorate

This report is published in the interest of scientific and technical information exchange, and its publication does not constitute the Government's approval or disapproval of its ideas or findings.

REPORT DOCUMENTATION PAGE

Form Approved
OMB No. 0704-0188

The public reporting burden for this collection of information is estimated to average 1 hour per response, including the time for reviewing instructions, searching existing data sources, gathering and maintaining the data needed, and completing and reviewing the collection of information. Send comments regarding this burden estimate or any other aspect of this collection of information, including suggestions for reducing this burden, to Department of Defense, Washington Headquarters Services, Directorate for Information Operations and Reports (0704-0188), 1215 Jefferson Davis Highway, Suite 1204, Arlington, VA 22202-4302. Respondents should be aware that notwithstanding any other provision of law, no person shall be subject to any penalty for failing to comply with a collection of information if it does not display a currently valid OMB control number. **PLEASE DO NOT RETURN YOUR FORM TO THE ABOVE ADDRESS.**

1. REPORT DATE (DD-MM-YY) May 2016			2. REPORT TYPE Final		3. DATES COVERED (From - To) 11 February 2014 – 10 February 2016	
4. TITLE AND SUBTITLE TQUID MAGNETOMETER AND ARTIFICIAL NEURAL CIRCUITRY BASED ON A TOPOLOGICAL KONDO INSULATOR			5a. CONTRACT NUMBER FA8650-14-1-7407			
			5b. GRANT NUMBER			
			5c. PROGRAM ELEMENT NUMBER 61101E			
6. AUTHOR(S) Jing Xia, Zach Fisk, and Victor Galitski			5d. PROJECT NUMBER 1000			
			5e. TASK NUMBER N/A			
			5f. WORK UNIT NUMBER Y0Y4			
7. PERFORMING ORGANIZATION NAME(S) AND ADDRESS(ES) University of California Irvine 5171 California Avenue Ste. 150 Irvine, CA 92617-3067			8. PERFORMING ORGANIZATION REPORT NUMBER			
9. SPONSORING/MONITORING AGENCY NAME(S) AND ADDRESS(ES) Air Force Research Laboratory Sensors Directorate Wright-Patterson Air Force Base, OH 45433-7320 Air Force Materiel Command United States Air Force			10. SPONSORING/MONITORING AGENCY ACRONYM(S) AFRL/RYDD			
			11. SPONSORING/MONITORING AGENCY REPORT NUMBER(S) AFRL-RY-WP-TR-2016-0070			
12. DISTRIBUTION/AVAILABILITY STATEMENT Approved for public release; distribution unlimited.						
13. SUPPLEMENTARY NOTES This report is the result of contracted fundamental research deemed exempt from public affairs security and policy review in accordance with SAF/AQR memorandum dated 10 Dec 08 and AFRL/CA policy clarification memorandum dated 16 Jan 09. The material is based on research sponsored by Air Force Research Laboratory (AFRL) and the Defense Advanced Research Agency (DARPA) under agreement number FA8650-14-1-7407. The U.S. Government is authorized to reproduce and distribute reprints for Governmental purposes notwithstanding any copyright notation thereon. The views and conclusions contained herein are those of the authors and should not be interpreted as necessarily representing the official policies or endorsements, either expressed or implied, of Air Force Research Laboratory (AFRL) and the Defense Advanced Research Agency (DARPA) or the U.S. Government. Report contains color.						
14. ABSTRACT This program focuses on experimental and theoretical investigations of a newly discovered class of materials BB topological Kondo insulators that have been theoretically predicted and experimentally discovered in Samarium hexaboride. The success of the first part of the proposed research project will result in an ultrasensitive TQUID magnetometer with fT magnetic field sensitivity, rivaling that of superconducting interference device (SQUID). Advantageous to cryogenic SQUID, a TQUID can potentially be constructed with room- temperature topological insulator materials. The success of the second part of the proposed research project will result in a new strategy for constructing artificial neuristor and neural network. The theoretical part of the proposed work will lead to a microscopic theory of electron interference, thermal transport and electron transport in a correlated topological surface state.						
15. SUBJECT TERMS quantum interference device, magnetometer, topological insulator						
16. SECURITY CLASSIFICATION OF:		17. LIMITATION OF ABSTRACT: SAR		8. NUMBER OF PAGES 44	19a. NAME OF RESPONSIBLE PERSON (Monitor) Mark Pacer	
a. REPORT Unclassified	b. ABSTRACT Unclassified	c. THIS PAGE Unclassified	19b. TELEPHONE NUMBER (Include Area Code) N/A			

Table of Contents

Section	Page
List of Figures	ii
List of Tables	ii
1.0 SUMMARY	1
2.0 RADIO FREQUENCY TUNABLE OSCILLATORS BASED ON SMB ₆ MICRO- CRYSTALS	2
2.1 Introduction	2
2.2 Fabrication of SmB ₆ Oscillator	2
2.3 32 MHz Oscillator Device	3
2.4 1 kHz Oscillator Device	4
2.5 Scaling of Operation Frequency and the Device Size	5
2.6 The Critical Role of Surface State for the Oscillator Device	6
2.7 The Theory for SmB ₆ Oscillator	7
2.8 Experimental Data of Sample 5	10
2.9 Agreement between Theory and Experimental Data	10
2.10 Possibility of Oscillator Fabrication with Other Materials	11
2.11 Performance Metrics of SmB ₆ RF Oscillator	12
3.0 SMB ₆ TQUID MAGNETOMETER	14
3.1 TQUID Magnetometer	14
3.2 Demonstration of TQUID Magnetometer with nT Sensitivity	16
3.3 Study of Magnetically Doped SmB ₆ to Understand the Cause of Limited Dephasing Length at Temperatures above mK	18
3.4 Growth of Other TKI Candidates to Search for Longer Dephasing Length	22
3.5 dHvA Quantum Oscillation Measurement	24
4.0 CONCLUSIONS	35
5.0 REFERENCES	36
6.0 RESULTING PUBLICATIONS	38
LIST OF ACRONYMS AND ABBREVIATIONS	39

List of Figures

Figure	Page
Figure 1: Device Fabrication	3
Figure 2: 32 Mhz SmB ₆ Oscillator.....	4
Figure 3: Low Frequency Device	5
Figure 4: Scaling of Frequency with Crystal Size	6
Figure 5: Modeling the Oscillation	8
Figure 6: Amplitude and Frequency Tuning via DC Bias Current and External Capacitor for Sample 5	10
Figure 7: Comparing the Model with Experimental Results	11
Figure 8: Quantum Interference and TQUID Magnetometer	15
Figure 9: Setup for Testing TQUID Magnetometer	16
Figure 10: TQUID at 20 mK.....	17
Figure 11: TQUID at 100 mK.....	17
Figure12: Determination of Magnetic Dopants using EDS	18
Figure 13: MR Data of Gd and Ce-doped Samples	19
Figure 14: Ce-doped Samples.....	20
Figure 15: (a) Temperature Dependence (> 500mK) for Doped SmB6 with Different Doping and Concentrations and (b) Temperature Dependence of Gd-doped SmB6 in zero, 6 T, and 12 T Applied Field.....	21
Figure 16: Arrhenius Plots for Doped and Undoped SmB ₆	22
Figure 17: Result of FeSb ₂ Crystal	23
Figure 18: Result of Ce ₃ Bi ₄ Pt ₃ Crystal	23
Figure 19: Result of LaFe ₄ P ₁₂ Crystal.....	24
Figure 20: Schematic for the Cantilever Construction	26
Figure 21: Cantilever for dHvA Measurements.....	26
Figure 22: Capacitance Measurement Circuit.....	28
Figure 23: dHvA Quantum Oscillation of SmB ₂ Crystals from 30 mK to 25 K Temperatures ..	30
Figure 24: FFT of dHvA Data of Pure and Impure Samples	31
Figure 25: Angular Dependence of dHvA Data	32
Figure 26: Resistance Measurements.....	33

List of Tables

Table	Page
Table 1. Key Performance Metrics of the Tunable Oscillators	12

1.0 SUMMARY

The aims of this project were to develop two devices utilizing the newly discovered surface state of SmB_6 : (1) a topological quantum interference device (TQUID) magnetometer based on interference on the topological surface state and (2) a high frequency oscillator device that can be later inter-connected to form circuits mimicking that of neural network.

Aim 2 was a complete success where we have achieved experimental demonstration and have developed a quantitative theory. There is potential to further increase the operation frequency to THz regime with micron-sized devices.

For aim 1, we have demonstrated a TQUID magnetometer device with nT magnetic sensitivity at mK temperatures. However, enhancing the operation temperature turned out to be a great challenge due to the diminishing dephasing length with rising temperatures. We have spent a lot of time trying to solve this unexpected problem: study of the effect of magnetic dopants, improving growth process to reduce the amount of magnetic impurity, and use quantum oscillation measurement to see if any change occurs at low temperature in the electronic property of the surface state. Although we have learnt quite some new physics, we have had limited success with increasing the dephasing length.

The project has resulted in 3 papers: “Topological Kondo Insulators” published in Annual Review of Condensed Matter Physics in 2016. “Radio Frequency Tunable Oscillator Device Based on SmB_6 Micro-crystal” has received favorable review at Physical Review Letters, and was also published in 2016. “Weak Anti-localization and Linear Magnetoresistance in The Surface State of SmB_6 ” is waiting for reviewer report.

In summary, in this project, we have demonstrated a radio frequency (RF) tunable oscillator device, perhaps the first real-life device of topological Kondo insulator. We have developed a quantitative theory that matches perfectly with experimental results. We have also demonstrated a TQUID magnetometer, although only working at mK extremely low temperatures due to limited dephasing length. The latter is likely due to physics that we don't yet understand.

2.0 RADIO FREQUENCY TUNABLE OSCILLATORS BASED on SmB₆ MICRO-CRYSTALS

2.1 Introduction

Radio frequency tunable oscillators are vital electronic components for signal generation, characterization, and processing. They are often constructed with a resonant circuit and a “negative” resistor, such as a Gunn-diode, involving complex structure and large footprints. Here we report that a piece of SmB₆, 100 micron in size, works as a current-controlled oscillator in the 30 MHz frequency range.

When biased with a few mA of direct current (DC), self-heating in SmB₆ causes a large nonlinear resistance, which could lead to oscillation behavior. In a prior paper (1) we found that mm-sized SmB₆ crystals coupled to an external capacitor generate alternating current (AC) voltages at frequencies up to kHz with a few mA of DC bias current. While we speculated that this oscillation behavior might be related to the coupled electric and thermal dynamics of SmB₆, the exact mechanism was not understood. This was in part because the surface state had not been discovered at that time, making correct modeling impossible. It was unclear how and if the intricate oscillations could be pushed to higher frequencies. With the recent advancements in the understanding of SmB₆, we are now able to develop a model with both the surface and bulk states. In this model, the origin of the oscillations lies in the strong coupling between the thermal and electrical phenomena in this surface-bulk system. Sufficient Joule heating, induced by an external DC current, can heat the bulk into a less insulating state, and trigger coupled temperature and current oscillations in both bulk and surface states. A full physics model of the oscillator is to be constructed later in this project. A semi-phenomenological model, the stability of the voltage across a SmB₆ crystal with both surface and bulk states depends on the stability of a Jacobian matrix constructed from two autocatalytic reactions: one from the thermalization process of surface/bulk electrons and the other from that of the RC circuit. In the end, the oscillation corresponds to a time-scale τ (1):

$$\tau \sim \left(\frac{1}{c} \left(\frac{1}{R} + \frac{\partial I_s}{\partial V_s} \right) \right)^{-1} \quad (1)$$

This model could describe various aspects of the oscillations well and predicts that the frequency will rise sharply with reduced SmB₆ surface area, which we found to be true in SmB₆ micro-crystals.

2.2 Fabrication of SmB₆ Oscillator

We used Al flux growth in a continuous Ar purged vertical high temperature tube furnace with high purity elements to grow all single crystals. The samples are leached out in sodium hydroxide solution. The surfaces of these crystals were carefully etched using an equal mixture of hydrochloric acid and water for one hour to remove possible oxide layer or aluminum residues. Samples used in the experiments were selected from a batch of samples based on their size. The exposed surfaces are (100) planes. Platinum wires are attached to the samples using a micro spot welding. Measurements were carried out in a cryostat (0.3 – 300 K) using a standard DC voltage supply and oscilloscope. Only the SmB₆ crystal was held at low temperature, while

all other components were held at room temperature. Low resistance wires connect the crystal to the current supply, capacitor, and oscilloscope in parallel.

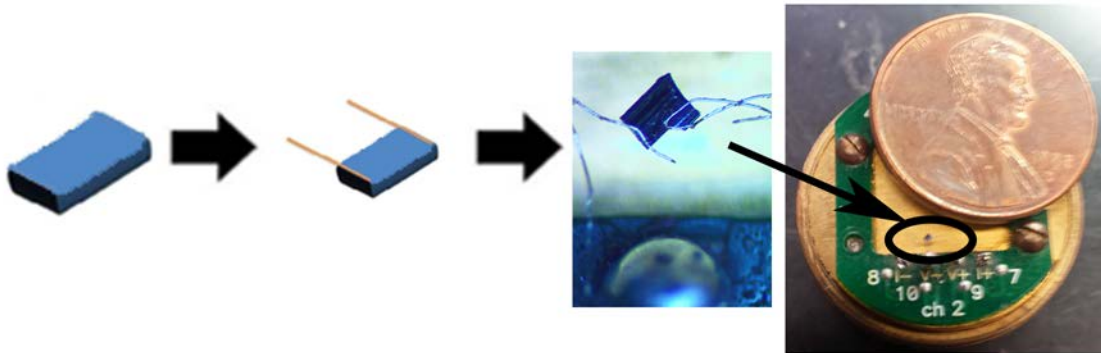


Figure 1: Device Fabrication

The steps are described in the text in more detail. Crystals are grown using the aluminum flux method and selected based on size with extra aluminum etched off with hydrochloric acid. Two platinum wires are spot welded on to the sample. Then the sample is mounted to the stage and inserted into the cryostat to be measured.

2.3 32 MHz Oscillator Device

Shown in Figure 2 is a 32 MHz oscillator device based on a 100- μm -sized SmB_6 micro-crystal. DC bias currents (I_0) up to 4 mA are applied through two platinum wires 25 μm in diameter that are spot-welded onto the crystal surface. And the output voltage is measured via the same platinum wires using an oscilloscope. The SmB_6 crystal itself is placed at low temperature in a cryostat, while other electronic components are held at room temperature outside the cryostat. If not explicitly stated, the measurements were performed when the cryostat is at 2 K.

For mm-sized SmB_6 crystals an external capacitor is required to generate oscillation, such an external capacitor is found to be unnecessary for micro-crystals described here, likely due to the self-capacitance we found in SmB_6 . The exact origin of the self-capacitance is still unclear, but it seems to scale with the surface area, suggesting its relevance to the surface state. The oscillation behavior doesn't depend on the exact geometry of the crystal: as shown the figure inset this oscillator is based on a rather irregularly shaped SmB_6 sample. The output of this oscillator can be continuously tuned from 29 to 35 MHz by varying I_0 between 0 and 4 mA. Shown in Figure 2(a) are outputs for three representative $I_0 = 0.47, 1.56$ and 2.42 mA. And the Fourier transformations are shown in Figure 2(b), showing a typical full width at half maximum (FWHM) spectral width Δf of only 0.05 MHz. We note that this is achieved without a phase-locked loop circuit.

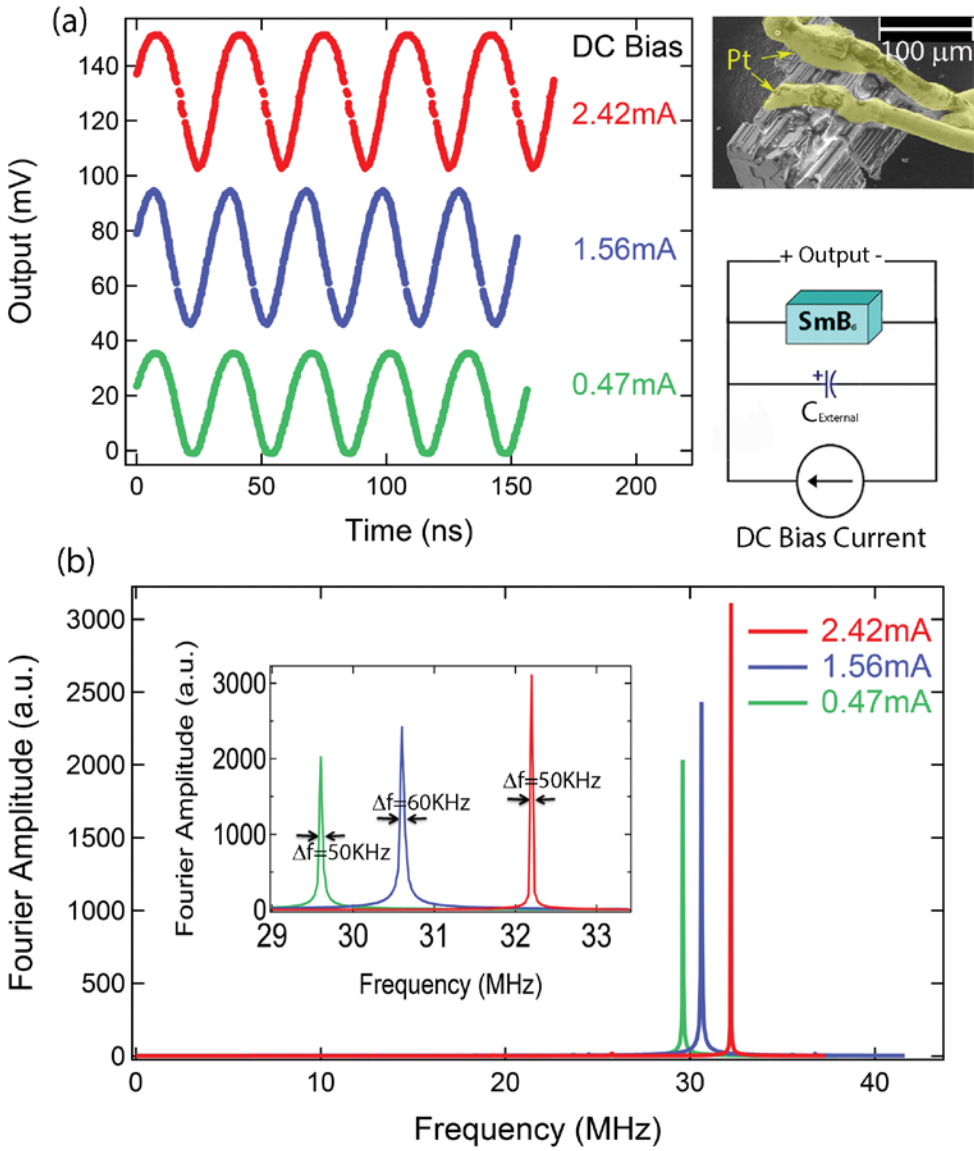


Figure 2: 32 MHz SmB₆ Oscillator

(a) Representative oscillation outputs at frequencies of 29.6, 30.6, and 32.2 MHz in ascending order, with DC bias currents of 0.47, 1.56 and 2.42 mA. Inset shows false-color electron microscope image of the device with platinum wires colored in yellow and SmB₆ crystal in white. The oscillator circuit consists of DC current flowing across the crystal and a capacitor (either an external capacitor or from the self-capacitance in SmB₆) in parallel. An oscilloscope is then used to measure the output waveform. (b) Fast Fourier Transform (FFT) of the data.

2.4 1 kHz Oscillator Device

For larger devices, the operation frequency is significantly higher. In Figure 3 we show the performance data of a 0.7 mm sized oscillator device. The center frequency can be tuned between 400 and 1000 Hz, much slower than the micro-device described in the last section.

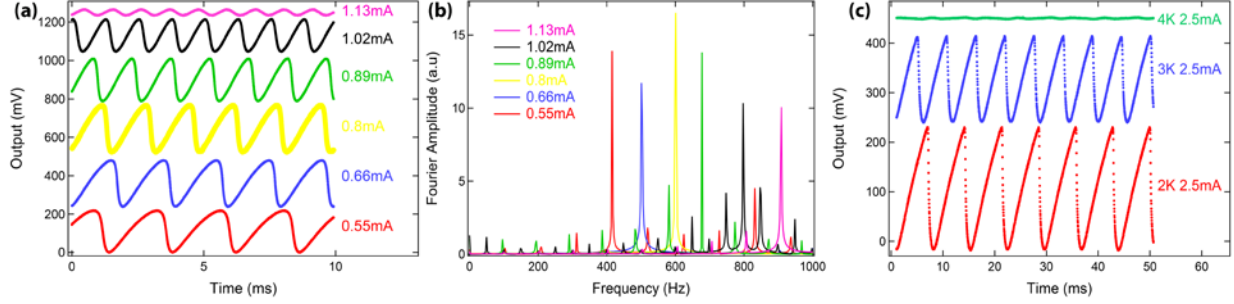


Figure 3: Low Frequency Device

(a) The time dependence of the oscillations. The waves become more sinusoidal and the frequency increases as the DC bias current increases. (b) The Fourier transform of the data in part a. The six peaks are shown to be sharp and far above other frequencies. (c) The time dependent oscillations at various temperatures. The oscillations disappear above 4K. A large capacitor was used in c than in a, which lowers the frequency and raises the allowable current.

2.5 Scaling of Operation Frequency and the Device Size

We find that the center frequency, which is the frequency where maximum oscillation amplitude occurs, rises quickly with smaller SmB_6 crystals. Plotted in Figure 4(a) are the center frequencies for a few representative oscillators of various sizes and geometries, versus their surface areas, which we found to show the highest correlation to center frequency, compared to volume or any single dimension. Projecting the frequency-surface area scaling further, we speculate that THz oscillations might occur for 10- μm -sized crystals. Operation above 2 THz is unlikely due to the 3.5 meV bulk activation gap in SmB_6 . For each device, a range of external capacitors can be used to generate oscillations, as illustrated in Figure 4(f), with no need for an external capacitor for the two highest frequency devices (29 and 32 MHz).

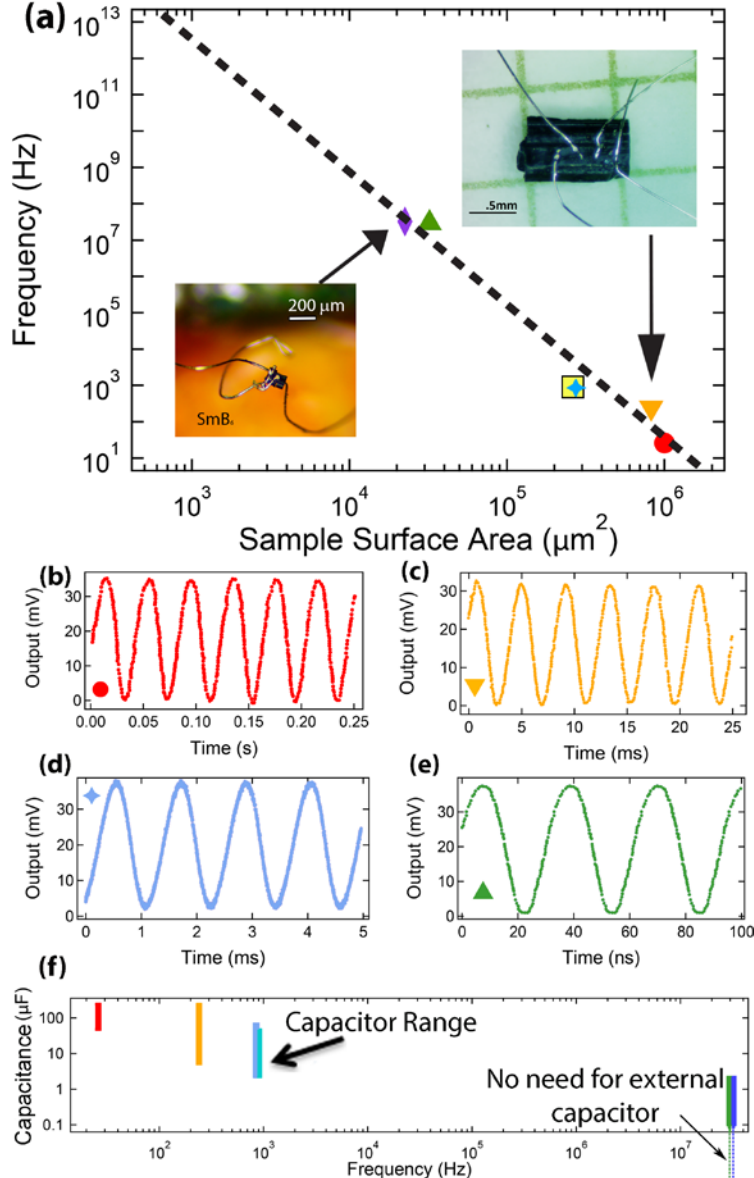


Figure 4: Scaling of Frequency with Crystal Size

(a) Center frequency of oscillator devices plotted against crystal surface area. Inserts are images of 29 MHz and 250Hz devices. The colors of the markers on this graph match the colors in b-e. (b-e) Output waveforms of the 25Hz, 250Hz, 1 kHz and 29 MHz devices respectively. The output of 32 MHz device is illustrated in Figure 1. (f) The range of external capacitance values we used for each device. No external capacitors are needed for the two highest frequency (smallest) devices.

2.6 The Critical Role of Surface State for the Oscillator Device

Both surface and bulk states are found to be essential for oscillation to occur. The oscillation amplitude diminishes at temperatures above 4 K, when bulk conduction dominates; or below 1 K, when surface conduction prevails. Optimal operation occurs at around 2 K when both the bulk and surface contribute to the electric conduction. It is known that in SmB₆, magnetic

dopants such as Gd destroy the conductive surface state (2), while inducing little change to the bulk insulating gap. We fabricated several devices using crystals from the same 3% Gd doped SmB_6 growth batch as described in (2). These Gd:SmB₆ samples are insulating to the lowest measurement temperature with no sign of a conductive surface. And the measured activation gap is found to be 3.3 meV, which is very close to the 3.4 - 3.5 meV bulk gap in SmB₆, suggesting its bulk is very similar to pure SmB₆. With the destruction of the surface state, no oscillation was observed from these crystals, despite testing a wide range of parameters such as temperature, bias current and external capacitance.

2.7 The Theory for SmB₆ Oscillator

We take into account both surface and bulk states we have built a model to describe the oscillations process depicted in Figure 3(d). It is based on charge and heat conservation equations and can be casted as follows

$$CR_S \dot{I}_S = I_0 - G I_S; \quad C_H \dot{T} = 2I_S^2 R_S G - I_S I_0 R_S - \gamma(T - T_0) \quad (2)$$

Here I_S and I_0 are surface and total currents through the sample; C is combined internal and external capacitance; $G = (R_S + R_B)/R_B$, where R_S and $R_B = R_B^0 \exp[-\Delta/T + \Delta/T_0]$ are the surface and bulk resistances with insulating gap Δ ; $C_H = C_H^0(T/T_0)^3$ and γ are the heat capacity dominated by phonons and heat transfer through external leads with temperature T_0 . C_H^0 and R_B^0 are heat capacity and bulk resistance in the thermal equilibrium. The detailed analysis of the model is presented in supplemental materials and here we outline our main results.

In dimensionless units the dynamics of the model depend on four parameters $\rho_B = R_B^0/R_S$, $\delta = \Delta/T_0$, $\Omega = C_H^0/\gamma CR_S = t_H/t_e$, and $i_0 = \sqrt{I_0^2 R_S / \gamma T_0}$, where $t_H = C_H^0/\gamma$ and $t_e = R_S C$ are time scales of thermal and electrical processes. The latter two can be easily tuned in the experiment by the DC bias current I_0 or capacitance C , and they control the behavior of the model. For the first two we use $\delta = 18$ and $\rho_B = 80$, which correspond to sample 5 at $T_0 = 2$ K. The system of equations (1) has only one fixed point (at which $\dot{I}_S = 0$ and $\dot{T} = 0$), which is not allowed to be a saddle one. The regime diagram of the model, presented in Figure 5, has the steady state regime, corresponding to a stable fixed point. The regime is separated by the Hopf bifurcation line from the limit-cycle regime, supporting nonlinear time-dependent oscillations of the current and the temperature and corresponding to an unstable fixed point. Figure 5(b) and (c) present the phase curves for the system (1), which illustrates the fate of the unstable fixed point, and the result of its explicit numerical integration. The oscillations, illustrated in Figure 3(d), can be separated into four phases: 1) Joule heating. The surface current achieves maximum, while temperature is minimum. 2) Discharging of capacitor. The energy flows from electrical to thermal. 3) Cooling phase. Energy dissipates to wire leads. The current is minimized, while the temperature is maximized. 4) Charging of capacitor. The energy flows from thermal to electrical. The system is open and non-equilibrium, but during the second and fourth phases the energy of the system is approximately conserved.

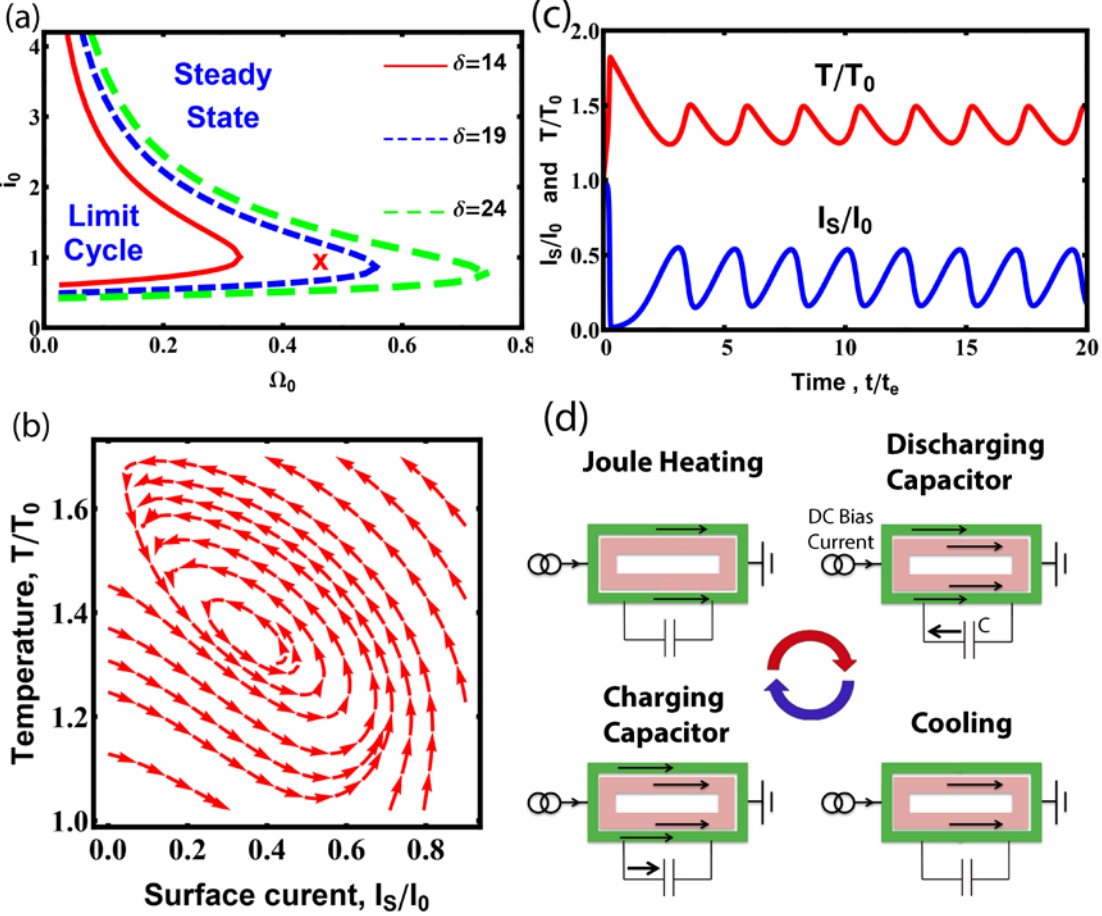


Figure 5: Modeling the Oscillation

(a) The regime diagram of the phenomenological model. The limit cycle regime supports nonlinear oscillations of temperature and currents. The red saltire symbol denotes the parameter set ($i_0 = 1.0$, $\Omega = 0.46$), for which time dependencies of the surface current and temperature, (c) and the corresponding vector flow plot, (b), for the model, described by the system (1), are presented. (d) Four phases of oscillations in order, which are described in the main text: Joule heating, discharging capacitor, cooling, and charging capacitor. The arrows represent the flow of current.

To describe voltage oscillations on the surface of SmB_6 we have developed a phenomenological model based on charge and energy conservation equations, which can be casted as follows:

$$CR_S \dot{I}_S = I_0 - G I_S; \quad C_H \dot{T} = 2I_S^2 R_S G - I_S I_0 R_S - \gamma(T - T_0) \quad (3)$$

Here I_S and I_0 are the surface and the total currents through the sample; C is internal or/and external capacitance; $G = (R_S + R_B)/R_B$, where R_S and $R_B = R_B^0 \exp[-\Delta/T + \Delta/T_0]$ are the surface and bulk resistances; the former is assumed to be temperature independent, while the dependence of the latter is crucial; $C_H = C_H^0(T/T_0)^3$ is the heat capacity, which is supposed to be dominated by the bulk phonons; C_H^0 is the heat capacity and R_B^0 is the bulk resistance in the

thermal equilibrium at temperature T_0 , while Δ is the energy gap in the insulating bulk; γ is the temperature independent heat transfer rate through external leads, which plays the role of the bath, and T_0 is their temperature. The system (3) needs to be supplemented by initial conditions. We assume that the surface current $I_S = G^{-1}I_0$ settles down without any delay, while the temperature $T = T_0$ is equal to the temperature of leads. The equations for the model (3) are nonlinear, have reach behavior and closely capture oscillations observed in the experiment.

In dimensionless units the dynamics of the model is controlled by four parameters $\rho_B = R_B^0/R_S$, $\delta = \Delta/T_0$, $\Omega = C_H^0/\gamma CR_S$, and $i_0 = \sqrt{I_0^2 R_S/\gamma T_0}$. The former two are not tuned in experiment, and weekly influence the behavior of the model. The latter two can be easily tuned by the current I_0 or capacitance C , and they control the behavior of the model. They can be rewritten as $\Omega = t_H/t_e$ and $i_0 = I_0/I_Q$, where $t_H = C_H^0/\gamma$ and $t_e = R_S C$ are the time scales of the electrical and thermal process, while $I_Q = \sqrt{\gamma T_0/R_S}$ is the current sufficient to change the temperature to $\Delta T \sim T_0$. For numerical calculations we fix the first two parameters as $\delta = 18$ (it corresponds to temperature $T=2K$), and $\rho_B = 80$ (it originates from the fitting for the sample 5). It should be noted that the value of ρ_B cannot be directly extracted from the experimental data, since the depth of sample which temperature is affected by currents is unknown. From the value $\rho_B = 80$ we estimate the depth as $d \sim 2.1$ mkm.

The system of equations (3) has *only* one fixed point (at which $\dot{I}_S = 0$ and $\dot{T} = 0$), which is a solution of the equation $i_0^2 = G(T - T_0)/T_0$. In the vicinity of the fixed point the system (1) can be linearized and is given by

$$CR_S \Delta I_S \dot{=} -G \Delta I_S - \frac{I_0 R_{SB}}{R_B} \frac{\Delta}{T^2} \Delta T; \quad C_H \Delta \dot{T} = 3 I_0 R_S \Delta I_S + \frac{2 I_0^2 R_{SB}^2}{R_B} \frac{\Delta}{T^2} \Delta T \quad (4)$$

with $R_{SB} = R_B R_S / (R_S + R_B)$ and the corresponding matrix we denote as \widehat{M} . According to the general theory of dynamical systems with two degree of freedoms ¹, the behavior of the system in the vicinity of a fixed point is defined by the signs of $\det \widehat{M}$ and $\text{tr } \widehat{M}$. It can be shown explicitly, that $\det \widehat{M} > 0$ and the fixed point of the model is not allowed to be a saddle one. The value of $\text{tr } \widehat{M}$ can be positive (unstable spiral or nod), negative (stable spiral or nod), and the transition between these two regimes, $\text{tr } \widehat{M}=0$, corresponds to the Hopf bifurcation. The stable fixed point corresponds to the steady state to which the system relaxes, while from the unstable fixed point the system flows to the limit-cycle behavior, which supports nonlinear time-dependent oscillations of the current and the temperature. The phase diagram of the model is presented in Figure 5(a) for different values of the parameter δ . Its area is dominated by the steady state, and only appears for a rather narrow range of parameters for the limit-cycle behavior. It appears only in an interval of currents $i_0^{c1} < i_0 < i_0^{c2}$ and only for $\Omega < \Omega^c$. The former condition demands Joule heating, induced by the currents, to be enough strong, $i_0^{c1} \leq i_0$, to make the bulk conductive. Nevertheless, if the system is overheated, $i_0^{c2} \leq i_0$, the bulk current dominates and oscillations do not appear. The latter condition implies that the time scale of thermal processes is smaller than the scale of electrical processes, which makes possible their coupled behavior. Phase boundaries $i_0^{c1}, i_0^{c2}, \Omega^c \sim 1$ depend explicitly on parameters δ, ρ_B , while the general structure of the regime diagram is insensitive to them. The phase curves for the

system (3), which illustrate the fate of the unstable fixed point and the appearance of the limit-cycle behavior, are depicted in Figure 5(b). Results of the explicit numerical solution of the system in the limit-cycle regime are presented in Figure 5(c).

Nonlinear oscillations appear in a rather narrow range of parameters and need fine-tuning. Redistribution of current between bulk and surface is crucial and temperature oscillations should be strong enough to change the hierarchy of the surface and bulk resistances. They are supplemented by oscillations of energy between electrical and thermal states and the corresponding times should match each other. These conditions are not easy to be satisfied. The bulk of the material does not need to be topologically nontrivial, and Dirac nature of the surface states is unimportant here, nevertheless topological Kondo insulator SmB_6 is the playground where all conditions required for the effect are naturally satisfied.

2.8 Experimental Data of Sample 5

We first show in Figure 2 the experimental data of sample 5. The output frequency and amplitude can be tuned by external capacitor and drive DC current, as shown in Figure 6(a) and (b) respectively. We choose this sample for the comparison with theory because it has a more regular shape that makes it easier for the calculation.

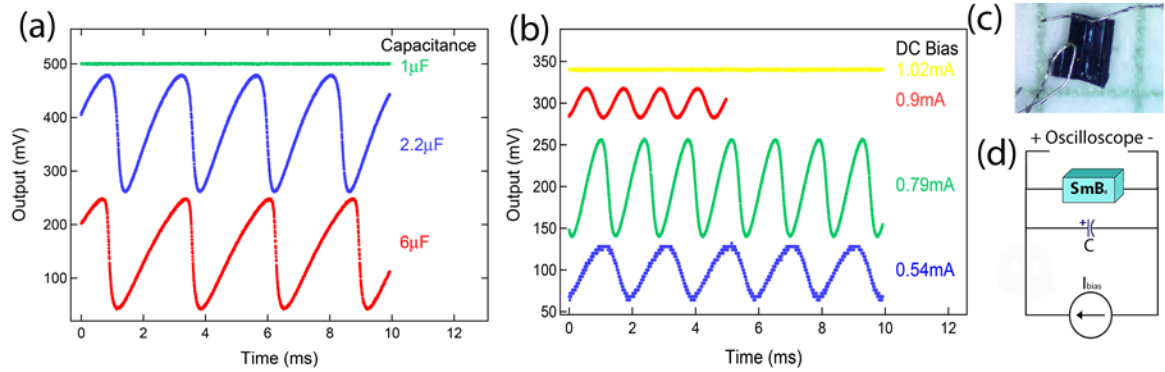


Figure 6: Amplitude and Frequency Tuning via DC Bias Current and External Capacitor for Sample 5

(a) The dependence of capacitance on the output. Decreasing capacitance increases frequency until the oscillations vanish. (b) The dependence of DC bias current on the output. (c) the device used for these measurements, which is less than 1mm in all spacial directions. (d) The schematic use to measure the oscillations.

2.9 Agreement between Theory and Experimental Data

In Figure 7 we compare the modeling results with experimentally measured oscillation behavior in sample 5. As shown in Figure 7(a) and (b), oscillations appear if the capacitance is larger than the minimal value C^c and only in a finite interval of currents, $I_0^{c1} < I_0 < I_0^{c2}$, which corresponds to conditions $i_0^{c1} < i_0 < i_0^{c2}$ and $\Omega < \Omega^c$ in our model (1) according to the regime diagram in Figure 3(a). Illustrated in Figure 4(c) and (d), between I_0^{c1} and I_0^{c2} the dependence of the frequency on the current is linear, while the dependence of the amplitude has a bell-shaped dependence. For a fixed DC bias current, the amplitude of the oscillations increases with

capacitance until saturation, while the frequency smoothly decreases. The critical values of currents and capacitance differ from sample to sample, but the behavior is general for all of them. According to our model, the oscillation frequencies are given by the inverse time scale $t_H^{-1} \approx t_e^{-1}$, which drastically decreases with sample surface area, in agreement with the experimental trend (Figure 4(a)).

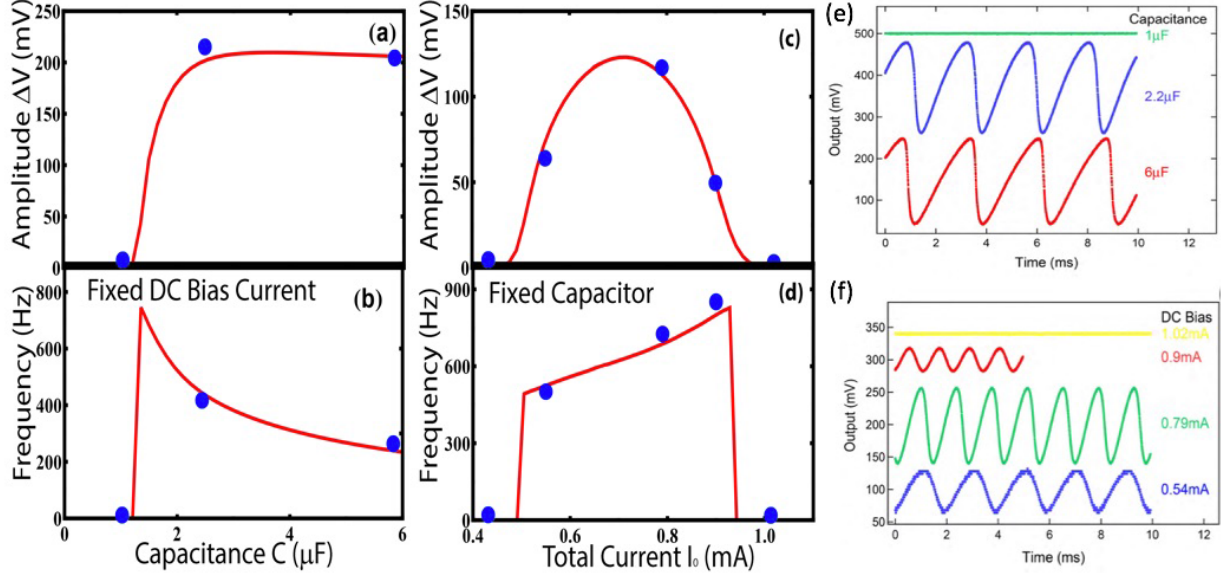


Figure 7: Comparing the Model with Experimental Results

(a) - (d) Red curves are predictions from the model. Blue dots are measured values from sample 5. The raw experimental data is shown in (e) and (f). Amplitude, ΔV , and frequency, ν , of the voltage oscillations on capacitance C for fixed DC bias current, I_0 , through the sample.

Blue dotted points correspond to $I_0^{exp} = 0.55$ mA, while red lines correspond to $I_0^{fit} = 0.76$ mA. (c) and (d), Amplitude ΔV , and frequency ν , of the voltage oscillations on DC bias current I_0 , through the sample for fixed capacitance C . The blue dots correspond to $C^{exp} = 2.2$ μ F, while red lines correspond $C^{fit} = 1.5$ μ F.

2.10 Possibility of Oscillator Fabrication with Other Materials

While the major focus of this paper is on oscillators operating at low temperature based on proposed topological Kondo insulator SmB_6 , the model developed here, in fact, describes a general system of a semiconductor and a metallic channel thermally and electrically coupled together. It is therefore in principle possible to realize such a tunable oscillator in other materials and at ambient temperatures. Candidate systems are $\text{Be}_2\text{Se}_3/\text{Bi}_2\text{Te}_3$ topological insulators, or less-exotic semiconductor quantum well heterostructures with two-dimensional electron gas. Consider a quantum well embedded in undoped narrow-band semiconductor InAs sample with length $l \sim 1$ μ m, width $d \sim 1$ μ m and height $h \sim 1$ μ m. At room temperatures $T \approx 300$ K undoped InAs has resistivity $\rho_B = 0.16$ Ω sm, heat capacitance $C_H^0 = 0.25$ J/(g K), heat conductivity $W = 0.27$ J/(s sm K), and density $\rho_D = 5.62$ g/sm³. As a result for a typical resistance of two-dimensional electron gas $R_S = 500$ Ω , the condition $R_S \approx R_B$ is satisfied. The parameters of our model, given by equations (1), can be estimated as $\gamma = Wld/h \approx 27 \cdot 10^{-6}$ J/sK and $C_H =$

$C\rho_D l dh \approx 1.3 \cdot 10^{-6} \text{ J/K}$. The first condition $\Omega \sim 1$ is satisfied if the time of thermal processes $t_H \approx 56 \text{ ns}$ matches the time of electrical processes $t_e = R_S C$, which can be achieved for a capacitance $C = 0.1 \text{ nF}$. The second condition, $i_0 \sim 1$, is satisfied for electric current $I_0 \approx (\gamma T / R_S)^{1/2} \approx 4 \text{ mA}$. The observation of oscillation in this nanostructure may demand fine-tuning of parameters; nevertheless we are optimistic that the conditions can be satisfied at room temperature.

2.11 Performance Metrics of SmB₆ RF Oscillator

We summarize a few key performance metrics of the tunable oscillators developed in this project, in comparison with other existing technologies. The details of performance metrics are discussed after the table.

Table 1. Key Performance Metrics of the Tunable Oscillators

	SmB ₆ current-controlled oscillator	Quartz-based tunable oscillator (Mini-Circuits POS 25)	MEMS-based tunable oscillator	Gunn diode-based tunable oscillator
Size	< 200 μm (10 μm for potential THz operation) Simple construction with just 1 crystal and 4 wires	> 1 mm quartz resonator 20 mm for full package	1 mm (SiTimes TM packaged device) 5 cm (3)	a few cm in size
Energy Usage	< 0.05 mW	200 mW	0.080 mW (3)	1 W
Price	< \$0.01 per piece in mass production due to simple construction and small size	\$16.95	\$ 10 (SiTimes TM packaged device)	\$100
Resilience against mechanical shock	No effect	Problematic due to mechanical nature	Better than quartz oscillator(4)	No effect
Resilience against damage	“Self-healing” due to topological protection of surface state	Will stop working	Will stop working	Will stop working

Size: We have fabricated and studied SmB₆ oscillator devices of various sizes from a few mm down to as small as 150 $\mu\text{m} \times 200 \mu\text{m} \times 50 \mu\text{m}$. The latter is already comparable (if not smaller) in size with the smallest quartz or MEMS voltage controlled oscillators. Since the device works through rapid thermal cycling between surface state and bulk state driven by the external current, the thermal mass of the region between the current leads would govern the frequency scale. Indeed both experimental and simulation results suggest that the central frequency scales as an inverse power law with the “effective” surface area between the two input leads on SmB₆ crystal.

Since the bulk energy gap of SmB_6 is equivalent to 5 THz radiations, we expect that the highest frequency we can achieve with this type of oscillator will be in the low THz range. This corresponds to 10 μm sized crystal. Based on these, we plan to fabricate THz devices with a $10 \mu\text{m} \times 10 \mu\text{m} \times 10 \mu\text{m}$ SmB_6 crystal and four 1- μm -wide lithographically patterned drive/output leads. This will be the smallest (and the simplest) tunable high frequency oscillator to our knowledge.

Price: Due to the extremely simple construction of the oscillator device (one crystal and four wires), the major cost comes from two parts: material, and wire bonding. The material comes mostly from SmB_6 itself. In our lab, it costs about \$1000 to produce 1 gram of high quality SmB_6 crystal including both raw element and labor. For a 10 μm size oscillator device, the weight is about 5×10^{-9} gram. Therefore the price is negligible. Four wire bondings are needed to construct a device, we estimate that it will cost \$1 if they are performed manually. And the cost will be reduced to less than 1 cent if performed with industry scale automatic bonders.

Resilience against mechanical shock: One advantage of the oscillator described here over quartz(5) and MEMS-based(4) tunable oscillators is that it is completely insensitive to mechanical shock. Unlike mechanical resonators, the SmB_6 oscillator doesn't involve any moving parts.

Resilience against damage: Our oscillator device consists of only a crystal and four wires. And it works as a current-controlled oscillator. Quartz and microelectromechanical systems (MEMS)-based voltage-controlled-oscillators (VCO) require additional micro-electrical components (6), which can be damaged by electric voltage outrage or mechanical shock. In the extreme case, even when the SmB_6 crystals are cracked mechanically, we found that our oscillator still functions as the surface state of SmB_6 reappears after damage as a result of topological protection. This is a unique advantage of the oscillator described here.

Energy usage: The energy is used to drive the mass in the “effective area”, which is between the two current leads to a thermally non-stable “limit cycle” regime. Therefore the energy usage inversely scales with the effective area of the device. For our kHz device (0.7 mm wide), the power is 2 mW. It is quickly reduced to 50 μW with the 50 MHz device (200 μm wide). This is already comparable to the power consumption of MHz Quartz and MEMS-based resonators. It is also anticipated that the energy usage of 10 μm sized THz SmB_6 oscillator under development would be below 1 μW , which is a very low power level.

3.0 SmB₆ TQUID MAGNETOMETER

3.1 TQUID Magnetometer

An improved SmB₆ surface would have important impacts on surface quantum interference and related weak anti-localization (WAL) effect. As illustrated in Figure 8(a), two types of electron interference exist in the surface state: the Aharonov-Bohm (AB) interference with two opposite electron paths finish a loop together; and the Altshuler-Aronov-Spivak (AAS) interference of two time-reversed counter-propagating electron paths. (A recent review in the context of topological surface state see (7)). Both interferences persist for multi-connected surface (8), e.g. that of a cylinder (Figure 8(a)), and give a quantum correction to the resistance of the cylinder. The phase difference of the interference is controlled by the enclosed magnetic flux Φ in units of flux quantum Φ_0 . Apart from magnetic flux, the nontrivial Berry phase of π for the topological surface state due to spin-momentum locking would result in destructive AAS interference at zero field. For a planar topological surface, the virtual AAS interferometers would give rise to enhanced conduction at zero magnetic fields (a review see (8)). This is called WAL effect, which has been studied extensively in Bi-based topological insulator (TI) materials (9-14). In SmB₆, we have recently measured the WAL effect indicating spin-momentum locking. We have extracted the length scale of dephasing (L_ϕ) and its temperature dependence from WAL measurements. As shown in Figure 8(b), we found L_ϕ follows a power-law behavior indicating electron-electron interaction as the main dephasing mechanism (8) below 100 mK. Thus at least at low temperatures, WAL can be used to probe electron interaction. In particular, we plan to use WAL to probe the dephasing due to the introduction of “Kondo holes” (7, 15) (non-magnetic impurities). These Kondo holes would interact with surface electrons via Kondo effect (8, 16), giving rise to enhanced scattering. We have shown that with 3-5% of Y or Yb nonmagnetic doping, the surface state still persist (2, 17, 18), giving two ideal systems for such a study. Another interesting aspect of WAL is that each independent surface band would contribute a fixed amount to the quantum correction to conductivity, as described by Hikami-Larkin-Nagaoka (HLN) equation (7, 19) in the limit of long inelastic scattering time. We found in SmB₆ that the size of WAL signal on the (100) surface can be fully accounted for by one channel. Considering the three Dirac bands as predicted by theory (9-14, 20, 21) and observed by angle resolved photoemission spectroscopy (ARPES) (8, 22-24), it suggests that the three surface bands have strong inter-scatterings and/or have very different dephasing lengths (25). We note that varying the amount of structural defects will most dominantly affect the former, providing a method we will utilize to see which scenario is correct.

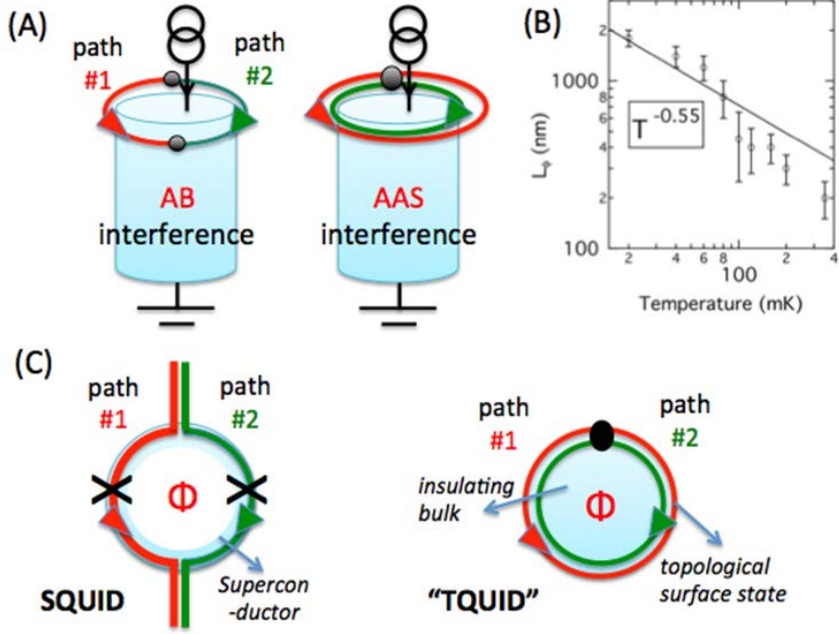


Figure 8: Quantum Interference and TQUID Magnetometer

(a) *AB vs. AAS interference on the surface.* (b) *Dephasing length obtained from WAL measurements.* (c) *SQUID vs. TQUID magnetometers.*

With L_ϕ measured, one can explore AB interference from micron-sized SmB_6 rods, whose circumference is comparable to L_ϕ to maintain phase coherence. Such measurements have been performed in Bi-based TI nano ribbons (14, 26, 27) giving direct information regarding nontrivial Berry phase. Mechanically crashing SmB_6 crystals sometimes creates plates with a cross-sectional length of the order of L_ϕ . We can explore AB interference experiments in these small samples at mK temperatures. To ensure thermal anchoring of the small samples, experiments will be carried out in a liquid Helium cell installed in our dilution fridge with samples immersed in liquid and wires connected to Ag sinters immersed in liquid too. Such a configuration has been found to be very effective in our lab for the base temperature of 15 mK, and has been proven to be sufficient even at 5 mK (28). The AAS interference, which is the basis for WAL, doesn't need to be restricted to micron-sized rods. Since the two paths of electrons travel exactly the same path but opposite directions, the absolute path length doesn't introduce decoherence. The only path difference comes from magnetic flux Φ and the Berry phase. The situation is very much like an optical fiber Sagnac interferometer (29, 30), in which low coherence lights ($L_\phi < 1$ mm) were used to interferer after traveling hundreds of meters of time-reversed paths. Just like in a fiber Sagnac interferometer (29), in a SmB_6 rod surface the back-scatterings from defects would create "ghost" interferometers that would wash out the interference pattern. However, the back scattering is quenched due to spin-momentum locking. Small angle scattering can still occur but will be averaged out in such a "multi-connected" geometry (8). A topological Kondo insulator (TKI) bar with mm^2 cross section is thus feasible with an interference period of a few nano-Tesla, acting as a magnetometer. In fact this is very similar to the workings of a superconducting quantum interference device (SQUID) magnetometer (31) as shown in Figure 8(c), and could in principle achieve comparable sensitivity. The sensitivity of the TQUID magnetometer is ultimately set by the cross-section of the device. For mm-sized samples, it could achieve similar sensitivity to SQUID if good

interference fringe visibility can be achieved. The fringe visibility depends on the ratio between surface state dephasing length L_ϕ and device size. Therefore, we need to improve sample quality in order to enhance L_ϕ .

3.2 Demonstration of TQUID Magnetometer with nT Sensitivity

To measure the tiny resistance oscillation of TQUID device, we mount the SmB_6 rod shaped crystal on a dilution fridge sample stage surrounded by a small magnetic coil inside a superconducting magnetic shield. This ensures that our measurement is not affected by ambient earth magnetic field. The voltage from 0.1 mm wide SmB_6 rod is amplified by a cryo-amplifier at 4 K before it is measured by lock-in amplifier (Figure 9). The cryo-amplifier could amplify the signal voltage by 300 times. Since the lock-in amplifier itself has a voltage resolution of 5 nV, we could use this setup to measure as small as 10 pico-Vol voltage oscillation across the SmB_6 crystal as magnetic field is swept.

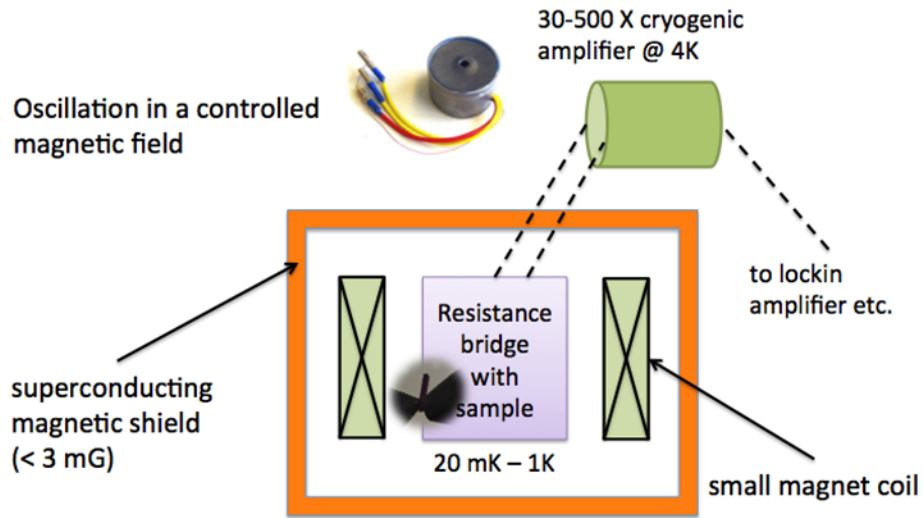


Figure 9: Setup for Testing TQUID Magnetometer

The voltage from 0.1 mm wide SmB_6 rod is amplified by a cryo-amplifier at 4 K before it is measured by lockin-amplifier.

With better quality of crystals, we measured the magnetic field induced resistance oscillation of a SmB_6 crystal with the cross section 160 μm by 200 μm , 2 mm long (i.e. a TQUID magnetometer). The performance at 20 mK temperature is shown in Figure 10: the magnetic field induced resistance oscillation is evident in this device with 50 nT period. We estimate that this is equivalent to 0.8 h/2e period. Since the interference fringe is quite visible, we think that 1 nT level magnetic field sensing is possible. Lots of knowledge is till need to be acquired before better devices can be made. The first is to figure out a reliable way to fabricate rod shaped crystals with high dephasing length. So far we have been hand selecting as-grown rod-shaped crystals, hoping it has good dephasing length. However, these crystals are rare. In the future we need to cleave the device out of large crystals. Therefore it will be important to figure out how cleaving changes dephasing length.

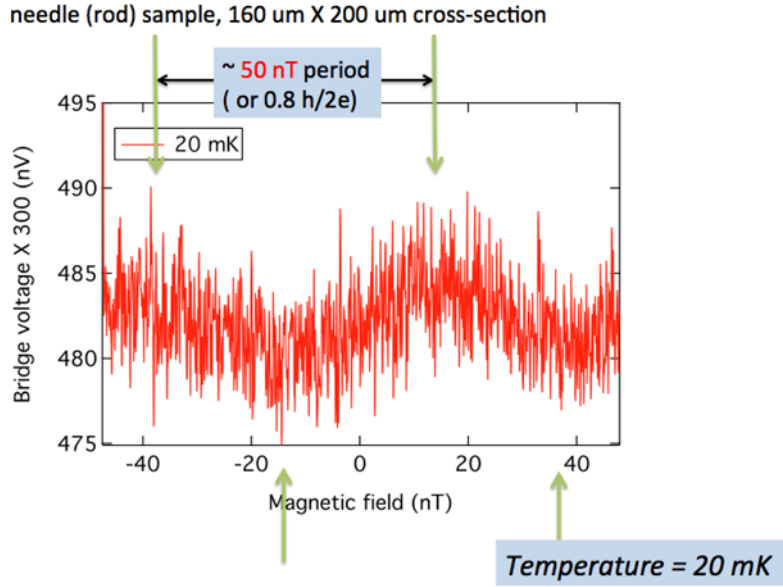


Figure 10: TQUID at 20 mK

Magnetic field induced resistance oscillation is evident in this device with 50 nT period. We estimate a practical magnetic resolution of 1 nT after some averaging.

Another important aspect of the device is its temperature dependence. As we have previously found, the dephasing length degrades rapidly as temperature is raised, due to electron-electron scattering. This results in degraded performance of TQUID performance. As an example, we show in Figure 11 the resistance oscillation at 100 mK. Although some oscillation can still be seen in the data, it is not sufficient to perform magnetic field sensing.

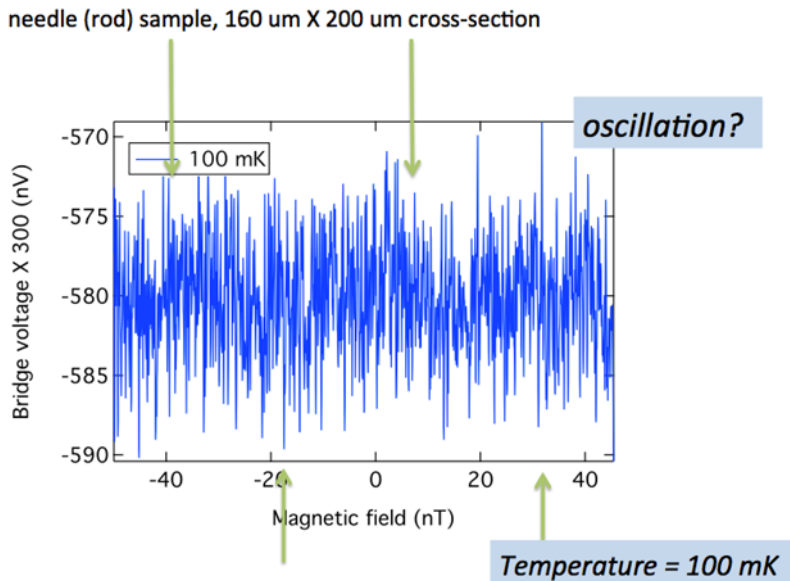


Figure 11: TQUID at 100 mK

Magnetic field induced resistance oscillation is barely visible.

3.3 Study of Magnetically Doped SmB₆ to Understand the Cause of Limited Dephasing Length at Temperatures above mK

With trace amount (< 0.1%) of either Gd or Ce dopants, the weak-anti-localization effect disappears completely, indicating that the dephasing length is reduced to essentially zero. This is why magnetic dopants are catastrophic to the TQUID magnetometer device. With > 3% of Gd dopants, the surface of SmB₆ becomes an insulator with an activation gap of 1.5 K. With > 3% of Ce dopants, the surface of SmB₆ is still metallic, but with additional scattering resembling that of Kondo effect.

Doping SmB₆ with low concentrations of non-magnetic impurities was previously shown to have no effect on surface conduction, whereas doping with Gd was found to lead to a non-metallic surface. Here, we further explore the effect of low concentrations of magnetic dopants in SmB₆. We find that Gd-doping results in the onset of insulating behavior below 2 K, best described by the opening of a second gap. Ce dopants act as incoherent Kondo scatterers which lead to an ln(T) resistance rise at lowest temperatures. This behavior is comparable with a similar ln(T) behavior that is observed in undoped SmB₆ attributed to Kondo holes coming from vacancies on the surface.

SmB₆ crystals doped with different concentrations of Ce or Gd atoms were grown using the standard Al-flux technique. Standard 4-point alternating current (AC) measurement techniques were used to measure electronic transport in fields up to 12 T and temperatures down to 100 mK. The actual concentration of magnetic impurities was measured using a Phillips XL-30 scanning electron microscope (SEM) with an energy dispersive x-ray spectroscopy (EDS) option (Figure 12).

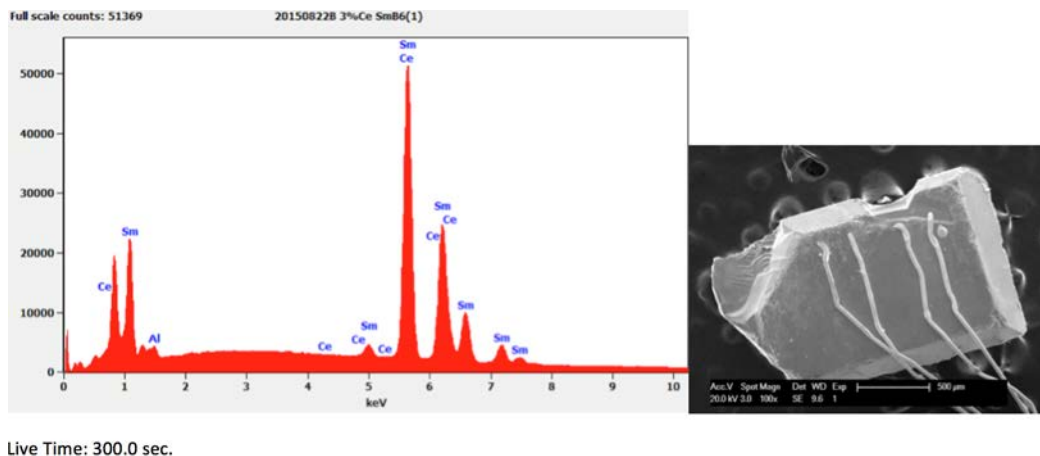


Figure 12: Determination of Magnetic Dopants using EDS
Left: EDS data of a 3% Ce doped SmB₆ sample and right: SEM image of the sample (with 4 gold wires for transport measurements).

The most striking difference between Gd and Ce dopants can be found in a comparison of the low-temperature magneto-resistance (Figure 13). Near zero field, Gd-doped samples exhibit a large peak in magnetoresistance (MR) that is quickly suppressed with applied field. The peak is not affected by the orientation of the sample with respect to an applied magnetic field, suggesting

that it is from the bulk. Fitting the low-field MR to the 3D weak localization model of Fukuyama and Hoshino with the approximation for $f_3(x)$ of Baxter provides a good fit to the data for fields less than .5 T. At higher fields the more gradual negative MR and eventual saturation might be attributed to Kondo scattering from Gd local moments. The saturation of this effect suggests that the impurity moments are fully aligned with the field at temperatures below 500 mK and fields above 9 T.

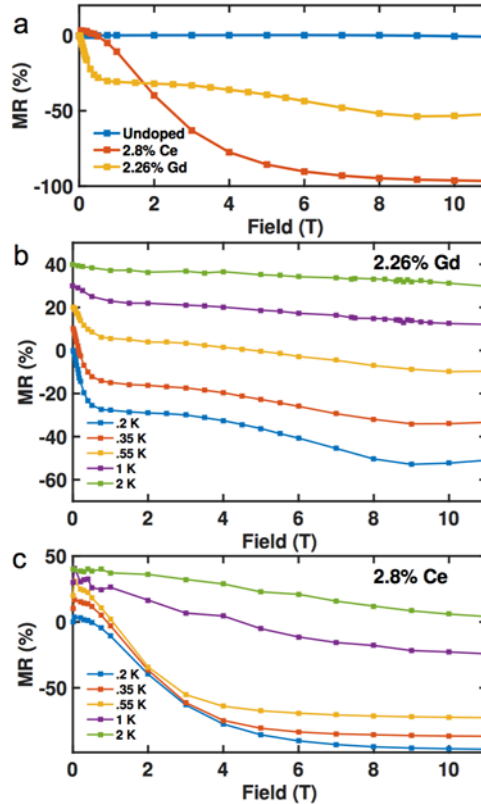


Figure 13: MR Data of Gd and Ce-doped Samples

(a) *MR of 2.8% Ce-doped, and 2.26% Gd-doped SmB6. Samples were measured at 200 mK. Magnetoresistance is calculated as: $[R(\mu_0 H) - R(0)]/R(0)$. Magnetoresistance of 2.26% Gd-doped (b) and 2.8% Ce-doped (c) SmB6 at several different temperatures. Each curve is offset from the previous curve by 10% for clarity*

Ce-doped SmB6 shows MR consistent with spin-1/2 Kondo scattering. Need functional form for magneto-resistance of spin-1/2 Kondo scattering. As the field is increased, the Ce local moments become polarized and the spin-flip scattering is reduced. This process should be independent of applied field direction, which was indeed observed for Ce-doped samples [see Figure 14(c) and (d)]. The saturation level of MR is sample dependent. This is because the total resistance is a combination of normal resistance Kondo term. The ratio of the two terms determines the amount of MR, and the Kondo term is highly sensitive to the concentration of magnetic dopants. It should also be noted that samples with higher doping show a small region with positive MR, with a peak near 0 T. This may be due to the beginnings of Kondo coherence of the Ce-ions as the concentration is increased. As the concentration is lowered this peak moves toward 0 T, and eventually the region of positive MR disappears.

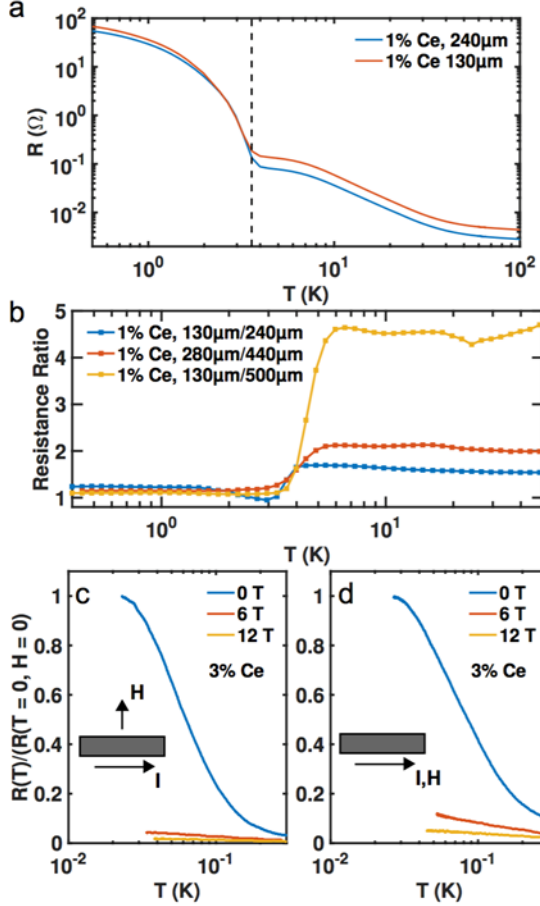


Figure 14: Ce-doped Samples

(a) *Resistance ratio between 1% Ce-doping.* For all samples there is a clear change from bulk dominated conduction above 6 K to surface dominated conduction below 3 K. Inset: Resistance value of 130 μm sample from the 130 μm/240 μm ratio in main plot. The dashed line shows where surface conduction starts dominating trans- port (3.6 K). (b) *Resistance of the sample measured at 240 μm and 130 μ. The dashed line is at the temperature (3.6 K) were the surface begins to dominate conduction.* (c) *Low- temperature resistance rise in 3% Ce-doped SmB6 with applied field perpendicular to the measuring current.* (d) *Same as (c) but with applied field parallel to the measuring current.*

One reason for the difference in MR arises from the fact that Ce-doping preserves the metallic surface state of un-doped SmB₆, whereas Gd-doping does not. We measured 0.8 single crystals of Ce-doped SmB₆ after polishing them into thin slabs and attaching leads for transport measurement via spot-welding. After performing measurement on the prepared crystals, the thickness of the crystal was carefully reduced without disturbing the previously attached leads by polishing the backside of the crystal. In a previous study, Gd-doping was shown to result in a non-metallic surface state via the same thickness-reducing procedure. In undoped SmB₆, it has been shown that the resistance saturation (and presumably surface conduction) persists in fields as large as 45 T. However, the large spin of Gd, resulting in a very strong local magnetic field, must allow the Gd dopants to break time reversal symmetry, causing the surface state to become gapped.

When cooled below 3 K, 1% Ce-doped crystals show a decrease in the resistance ratio to a value of nearly one, showing that surface conduction is dominating [see Figure 15(a)]. At higher temperatures, the ratio goes through a transition to a larger value, consistent with the ratio of the thicknesses of the crystals before and after polishing. For one of the crystals, the resistance of the sample increases by nearly two orders of magnitude below 4K. However, the ratio remains fixed at a value close to one, indicating that surface conduction is dominating transport. Thus, this large resistance rise must be attributed to a change in the value of the surface conduction (such a large extra rise in resistance is not present in undoped SmB_6).

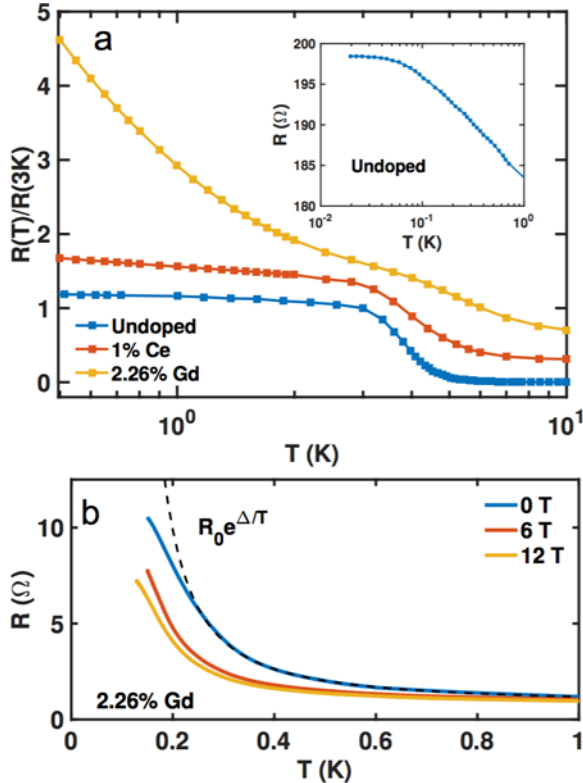


Figure 15: (a) Temperature Dependence ($> 500\text{mK}$) for Doped SmB_6 with Different Doping and Concentrations and (b) Temperature Dependence of Gd-doped SmB_6 in zero, 6 T, and 12 T Applied Field

Figure 15(a): The resistance is divided by the resistance at 3 K for easier comparison. Each curve is offset by .3 for clarity. Figure 15(b): The dotted line is a fit to activated behavior, with a gap of .53 K.

Adding dopants has minimal effects on the bulk gap [see Figure 16(a)], even up to 3% doping. For Ce, Gd, and Yb the bulk gap remains very close to 40 K. Below 3 K, the resistance of Gd-doped samples can be fit fairly well under the assumption of a second gap opening. For the sample in Figure 16(b) this gap has energy of 1.5 K. In a second sample, the temperature resistance can be fit to a gap of 1.53 K. Thus, the strength of the gap appears to be related to the concentration of dopants. The gap cannot be from the weak localization of the conduction electrons caused by the Gd dopants, because it is still evident at 6 and 12 T, well beyond the field range where weak localization is expected to occur. The origin of this second gap is unclear. The

MR data suggests that the bulk is dominating conduction at temperatures down to at least 200 mK.

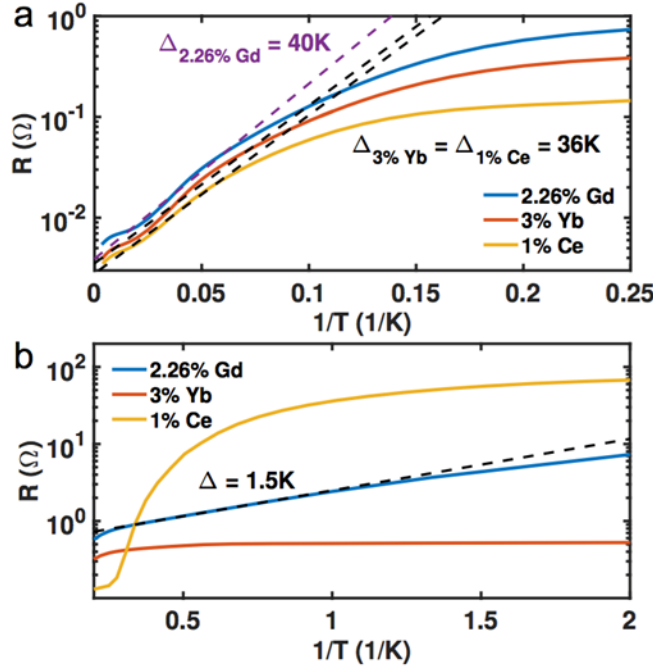


Figure 16: Arrhenius Plots for Doped and Undoped SmB₆

(a) High temperature region. Note that both the doped and un-doped samples fit fairly well to the same energy gap of 40 K. (b) Low temperature region. Undoped and Yb-doped samples show saturating behavior from surface conduction. The Ce-doped sample shows an increase in resistance that is not consistent with a second activated gap. The Gd-doped sample shows a secondary gap with energy 1.5 K. As the temperature is further decreased, the resistance shows signs of saturation

3.4 Growth of Other TKI Candidates to Search for Longer Dephasing Length

We have in the past year grown crystals of TKI candidates FeSb₂, Ce₃Bi₄Pt₃, and LaFe₄P₁₂. None of these samples shows convincing result of surface dominated conduction at low temperatures. We conclude that SmB₆ remains to be the only known TKI materials.

In Figure 17(a) we show the result of two FeSb₂ crystals. The residual resistance ratio (RRR) was measured to be 10,000, indicating unprecedented quality of the crystal. However, performing Hall measurement of two thicknesses down to T = 2 K, we found that the conduction is still dominated by the bulk (Figure 17(b)). There is no indication of a metallic surface state in FeSb₂.

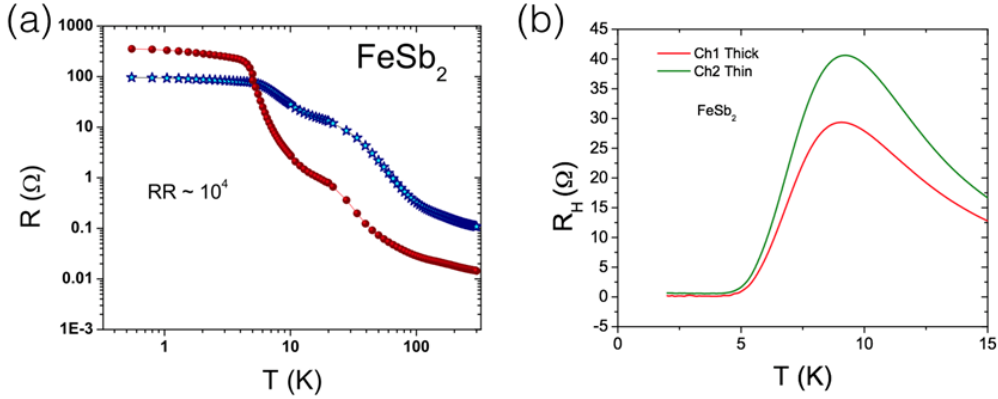


Figure 17: Result of FeSb_2 Crystal

(a) *Resistance vs. temperature for two samples with $RRR = 10,000$, indicating extremely good quality.* (b) *Hall coefficient vs. temperature for two thicknesses, showing that the conduction is still dominated by the bulk even at $T = 2$ K*

In Figure 18(a) we show the result of two $\text{Ce}_3\text{Bi}_4\text{Pt}_3$ crystals. The RRR was measured to be 1000, indicating unprecedented quality of the crystal. However, performing Hall measurement of two thicknesses down to $T = 0.4$ K, we found that the conduction is still dominated by the bulk (Figure 18(b)). There is no indication of a metallic surface state in $\text{Ce}_3\text{Bi}_4\text{Pt}_3$.

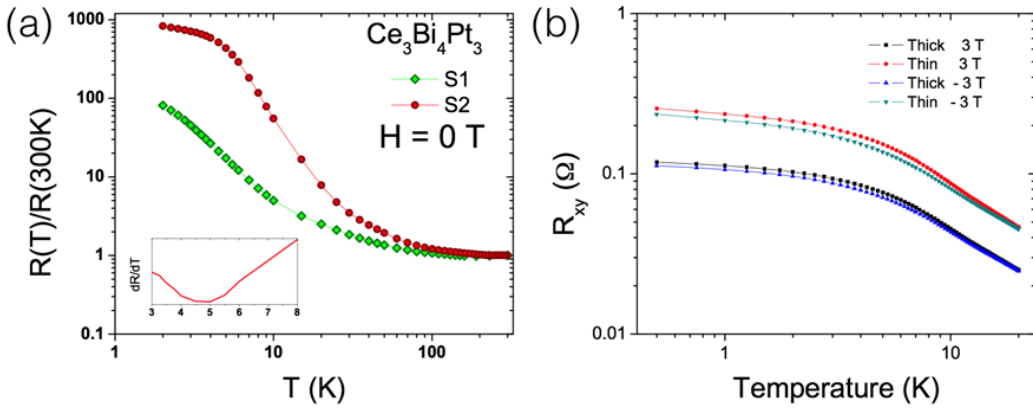


Figure 18: Result of $\text{Ce}_3\text{Bi}_4\text{Pt}_3$ Crystal

(a) *Resistance ratio of two crystals showing good sample quality and (b) thickness dependence of Hall resistivity. No indication of surface conduction was found down to $T = 0.4$ K.*

A few $\text{LaFe}_4\text{P}_{12}$ have been grown with relatively large sizes (0.1 mm). However, performing Hall measurement of two thicknesses down to $T = 0.4$ K, we found that the conduction is still dominated by the bulk (Figure 19). There is no indication of a metallic surface state in $\text{LaFe}_4\text{P}_{12}$.

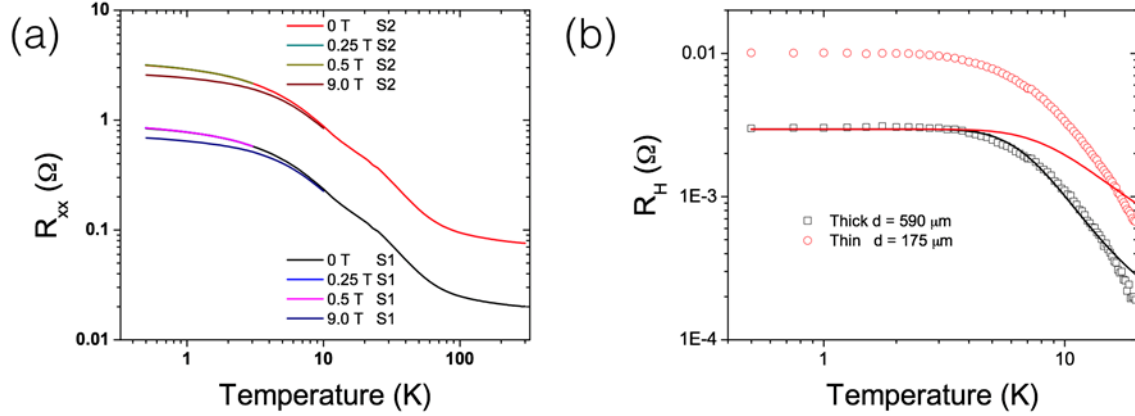


Figure 19: Result of LaFe₄P₁₂ Crystal

(a) *Resistance of two crystals and (b) thickness dependence of Hall resistivity. No indication of surface conduction was found down to $T = 0.4 \text{ K}$*

3.5 dHvA Quantum Oscillation Measurement

De Haas-van Alphen (dHvA) quantum oscillation measurement to verify the limited dephasing length is due to magnetic impurity instead of intrinsic change of surface electronic structure at temperatures higher than mK.

dHvA effects are quantum oscillations in the magnetization of a material due to changes in an applied magnetic field (32). In simplified terms, the external field limits the electronic states to a set of quantized tubes in k-space. Each tube has an area in a plane perpendicular to the magnetic field proportional to a quantum number times the magnetic field. As the field is varied, the outermost tube that is still inside the Fermi surface passes through the Fermi surface. As it does so, occupied states on that tube must relocate to tubes still inside the Fermi surface, changing the energy of the system, which manifests as a change in the magnetization. Onsager showed that the change in magnetization (among other properties) is periodic in $1/B$ and is related to the extremal areas of the Fermi surface in planes perpendicular to the magnetic field as follows (in SI units):

$$\Delta \left(\frac{1}{B} \right) = \frac{2\pi e}{\hbar} \frac{1}{A_e} \quad (5)$$

H is the applied magnetic field, and A_e is an extremal area of the Fermi surface. This phenomenon is particularly well suited for study via torque magnetometry because there is a torque on the sample as long as the extremal area of the Fermi surface varies with the direction of the applied field (i.e., the Fermi surface is not a sphere).

In an applied field, a magnetic dipole will experience a torque. Most crystals have an anisotropic susceptibility, so that the magnetization of the sample is not directly aligned with the applied field. The magnitude of the torque that such a sample would experience in a uniform field is:

$$\tau = M_{\perp} V B \quad (6)$$

Where M_{\perp} is the component of magnetization that is perpendicular to applied field, V is the volume of the sample, and B is the applied field. For a paramagnetic sample, the magnetization scales with the applied field. Thus, the torque acting on such a sample scales with the field squared. The scaling with applied field and volume of the sample makes torque magnetometry well suited for studying larger samples in high fields. In 2-dimensional materials, the magnetization will lie almost entirely along a single crystal axis (regardless of the direction of the applied field). In such systems, torque magnetometry provides a simple way to fully characterize the magnetization of the sample.

One method of performing a torque magnetometry measurement is by measuring the deflection of the free end of a beam cantilever on which the sample is mounted to determine the torque acting on the sample. If the cantilever is constructed from a metal foil, the deflection can be determined by measuring the change in capacitance between the cantilever and a fixed conductor. For small changes in deflection, the angle of the sample in the magnetic field will be nearly constant and the change in capacitance of the cantilever will be proportional to the torque acting on the sample. For large torque beyond the small deflection regime, one can use a feedback system to apply a known current through a loop on the cantilever to cancel the torque generated by the sample, but such an approach was not used here. Figure 20 shows a schematic view of a beam cantilever device mounted in the dilution refrigerator. Shielded cables are used to connect the cantilever to a current- balance circuit that can measure the change in capacitance of the cantilever sensor. Both the cantilever and the fixed conductor are electrically isolated from ground. To reduce the effects of stray capacitance, every other metallic surface in the cryostat should be grounded. Further, the shielding layer of the coaxial cable should be terminated as close to the cantilever device as possible. Because of the low dissipation (less than 10 fW) inherent in a vacuum-gapped capacitive measurement, it is possible to perform the measurement at mK temperatures. Using a lock-in amplifier capable of current measurement, the capacitance can be measured with sensitivity near 10 aF for sensors with total capacitance of 1 pF. As described in Huang et al.6, when measuring a high impedance device is it necessary use a current measurement method to reduce the effects of the stray impedance to ground. To increase the resolution of the measurement, a current-balance method was used to bias the measured current at the equilibrium position of cantilever near zero.

For a cantilever (shown in Figure 20) operating at mK temperature it is important to select construction materials with suitable electrical, magnetic, and thermal properties. It is also necessary to consider the geometry of the cantilever, which controls the spring constant and equilibrium capacitance. Figure 20 details the construction used for the cantilever. A picture of a representative cantilever with crystal sample on it is shown in Figure 21(a).

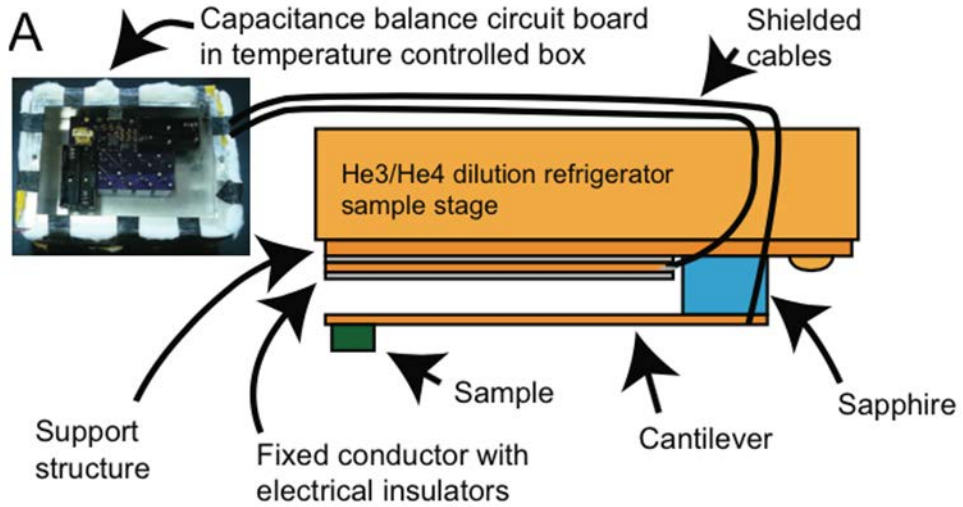


Figure 20: Schematic for the Cantilever Construction

The cantilever device is attached to a base plate that is suspended below the mixing chamber of a He3/He4 dilution refrigerator. Shielding cables from the device are routed out of the cryostat to the current-balance circuit.

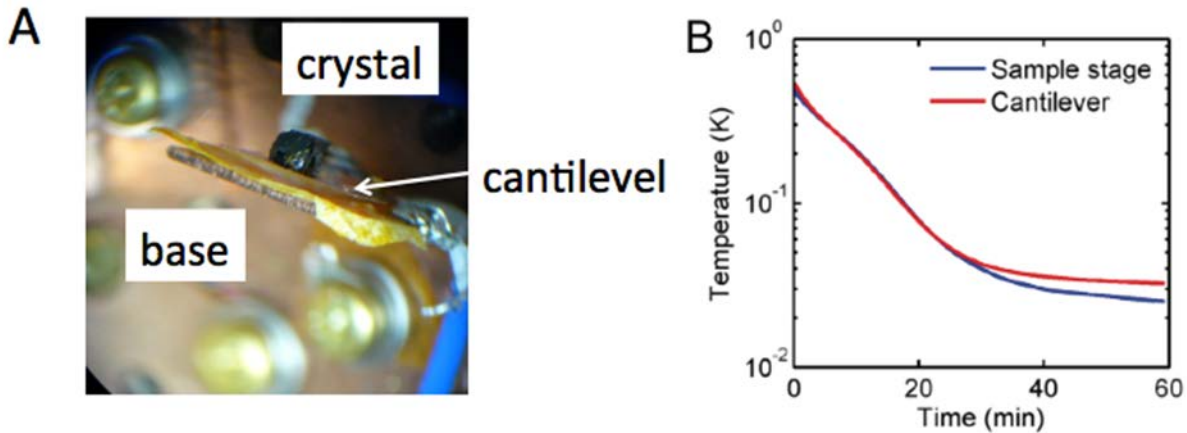


Figure 21: Cantilever for dHvA Measurements

(a) Close-up picture of cantilever, crystal sample and base plate and (b) the cantilever is well thermalized down to a very low temperature of 30 mK.

The cantilever was constructed on a .02 in thick oxygen free-high conductivity (OHFC) copper base piece that has a through hole drilled for mounting to the cryogenic sample stage attached to the mixing chamber in a dilution refrigerator. A cigarette paper was soaked in Ge-varnish and affixed to one end of the copper base. A thin copper foil was placed on top of the paper so that it is electrically insulated from the base. This foil serves as the fixed conductor. On the other end of the base a 435 μ m sapphire plate was affixed using low temperature epoxy (Loctite 1C Hysol). Using the same epoxy, a 35 μ m thick copper foil was affixed to the top of the sapphire plate to serve as the cantilever arm. Because the thermal conductance of the epoxy is much lower than that of sapphire or copper at mK temperatures, it is necessary to make the epoxy layer as thin as

possible. Ideally, some parts of the sapphire spacer should be in direct contact with both the cantilever and the base structure that is held at a fixed temperature through a heat link to the mixing chamber. The foil is cut into an I-shape, which allows for a smaller spring constant and also causes the motion of the free end of the cantilever to dominate the change in capacitance.

To protect against an electrical short, the fixed conductor was covered with a second piece of Ge-varnish soaked cigarette paper upon most of its surface except for a smaller corner to allow for an electrical contact to be made. Copper is a useful material for the cantilever because foils of the appropriate thickness are readily available in the form of tape. Although there are materials (e.g., brass) that are less diamagnetic than copper, the rolled copper foil has essentially zero magnetic anisotropy and therefore doesn't contribute a torque signal. Other materials, such as beryllium copper or kapton foils may be less subject to non-elastic deformation than copper, but have much lower thermal conduction. We found copper foil to be the best material for measurement at mK temperatures due to its thermal properties, resulting in quick cooling of the sample. The heat dissipated by the capacitance measurement is extremely low. For a typical sensor with a 1 pF equilibrium capacitance measured with a 2.5 V excitation at 2 kHz, the current through the device is only about 30 nA. With a vacuum-gapped capacitor, there is no lossy dielectric material in which heat is dissipated. Any device heating must be caused by ohmic losses in the wiring to the cantilever device, the solder joints, or in the copper foils that are used for the cantilever and fixed conductor. Even if the combined resistance were somehow as high as 10Ω , the total amount of heat dissipated would still be less than 10 fW, which is the level of heat generated by cosmic rays per gram of material. To check the sample temperature, a small ruthenium oxide thermometer (Scientific Instruments model RU600) was mounted to a cantilever device using Ge-varnish to mimic the sample. The thermometer was electrically insulated from the cantilever using a piece of Ge-varnish soaked cigarette paper. The electrical connection to the thermometer was made using thermally insulating manganin wires. It was found that the temperature of the cantilever and the sample stage remained nearly identical down to 50 mK (Figure 21(b)). After an additional 20 minutes of cooling, the temperature of the cantilever reached just over 30 mK. In an actual experiment, the sample is mounted directly to the surface of the cantilever, without the additional thermal barrier provided by the cigarette paper. Thus, it is likely that the thermal relaxation time and temperature of the sample may be even lower than that measured here.

The second task is to develop a circuit for high precision capacitance measurement. As shown in Figure 22(a) measurement of capacitance is performed using a current-balance method. An AC voltage from the lock-in amplifier output is applied to an audio transformer (Triad Magnetics TY-141P). The transformer output is center-tapped, with the center tap connected to electrical ground. The transformer output then acts like two AC voltage sources, each 180 degrees out of phase with the other. The voltage from one of the transformer outputs is passed across the cantilever device, while that from the other output is passed across a balance capacitor. The output from both the cantilever and balance capacitor are then joined at a common node that is connected to ground through the current input on a lock-in amplifier (or a current to voltage preamplifier). The current measured by the lock-in amplifier is proportional to the capacitance difference between the cantilever device and balance capacitor. To accommodate devices with a range of capacitance, a capacitance bank was added to the balance side of the circuit instead of a single capacitor. A range of balance capacitance can be chosen by connecting the appropriate set

of capacitors using jumper pins. When measuring changes of capacitance on the order of tens of aF, great care must be taken to eliminate unwanted sources of drift. To reduce the changes in stray capacitance due to relative motion of the wires and electrical components, we designed a PCB to join the necessary components. A small drift of 50 aF/h is achieved. For comparison, in the initial attempts at performing measurement the same circuit was built but with fairly flexible 22 AWG stranded copper wire. This resulted in a much higher drift near 1 fF/h. To reduce effects from thermal expansion, the electrical box containing the balance circuit was wrapped in an insulating material (aerogel). As shown in Figure 22(a), the whole box is held at a fixed temperature by attaching a temperature detector and heating element to the box inside to the insulation to provide temperature control. Temperature control was provided using a resistive temperature controller with stability of $+\/- .1$ $^{\circ}$ C/day. Finally, to reduce the effects of changes in relative humidity and water absorption by the printed circuit board (PCB), the component box was partially filled with a desiccating salt. Even though the drift was reduced to suitable levels for most measurements, residual drift on the order of 50 aF/h still exists, possibly from changes in the value of the reference capacitors (mainly due to changes in temperature) and changing stray capacitance between wires or traces in the system. NP0 capacitors have a tolerance in the temperature compensation of $+\/- 30$ ppm/ $^{\circ}$ K. For a 1 pF balance capacitor, this gives a worst-case change in reference capacitance of 30 aF/ $^{\circ}$ K. Thus, the drift due to changes in the value of the reference capacitance should be relatively minor.

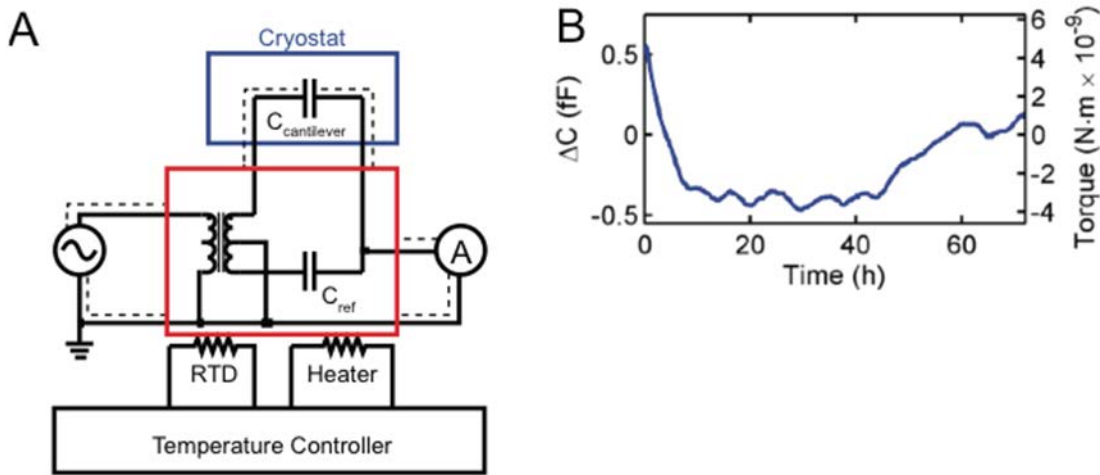


Figure 22: Capacitance Measurement Circuit

(a) *Circuit schematic for the current-balance capacitance measurement. The voltage source and ammeter functions are provided by the Signal Recovery 7225 Lock-in Amplifier. It is important that the shielded cables in the cryostat extend as close to the cantilever device as possible to avoid interference from other electrical signals in the cryostat.* (b) *Drift in measured capacitance versus time for the balance circuit. With environmental control of the current-balance circuit, the drift per hour is less than 50 aF after the temperature control has stabilized for 8 hours. Right axis: equivalent drift in measured torque assuming typical cantilever dimensions.*

Changes in the stray capacitances of the system from variance in the relative distance between wires or traces due to thermal expansion can have an impact on the measured capacitance. Typical capacitances between parallel traces are on the order of 10's of pF/m. The stray

capacitance for traces routed on top of each other between adjacent layers of a PCB is a similar order of magnitude. FR4 PCB, which was used for our capacitance balance circuit, has a coefficient of linear expansion near 13 ppm/°C for in-plane expansion. Along the z-axis, the expansion coefficient is over ten times larger. Assuming trace length of .5 m, trace width of .5 mm, and separation of 1.3 mm, the change in capacitance between parallel traces is about 40aF/°K. For a similar length of traces overlapping between layers, this effect is enhanced to near 500 aF/°K. In our completed system, the net effect of temperature drift was closer to 400 aF/°K as measured during a temperature sweep of the balance circuit near room temperature.

Topological insulators have recently attracted much attention due to their ability to host many exotic physical phenomena. The well-studied Kondo insulator, SmB6, exhibits surface metallicity and bulk insulating behavior at low temperatures. The measurement of quantum oscillations from the metallic surface state would provide information about the origin of the surface conduction and help investigate SmB6's surface property as a function of temperature. Single crystals of SmB6 were grown using the aluminum flux method. Samples were measured down to 2 K in a Quantum Design Physical Property Measurement System (PPMS), and down to 30 mK in an Oxford Instruments dilution refrigerator. Resistivity was measured using the standard 4-point technique. Magnetization was measured using cantilever-based torque magnetometry. AC susceptibility measurements were performed using a standard mutual inductance technique.

As a check on the origin of the oscillations, magnetoresistance at 50 mK was also measured on one of the samples that showed dHvA oscillations. After subtracting a polynomial background, the frequency content of the magnetoresistance was calculated. The lack of any clear peak in the frequency spectrum shows that Shubnikov-de Hass (SdH) oscillations are not detectable, even at 50 mK. This result is consistent with a recent magnetoresistance study on SmB6 as temperatures as low as 300 mK and using special contact structures to only measure the contribution for individual crystal surfaces.

To determine the effective mass of the observed dHvA oscillations, the temperature dependence of the oscillation amplitude was measured. The magnitude of the dHvA oscillations has temperature dependence given by the Lifshitz-Kosevich formula:

$$R_T = \frac{\alpha T m^*}{B} \sinh\left(\frac{\alpha T m^*}{B}\right) \quad (7)$$

Figure 23(f) shows a fit of the low-frequency oscillation amplitude at 8.3 T to the thermal damping equation. Using this fit, an effective mass of .101 m_e was obtained. This is consistent with the value reported by literature for their low-frequency α pocket when measured at an angle near the [100] axis.

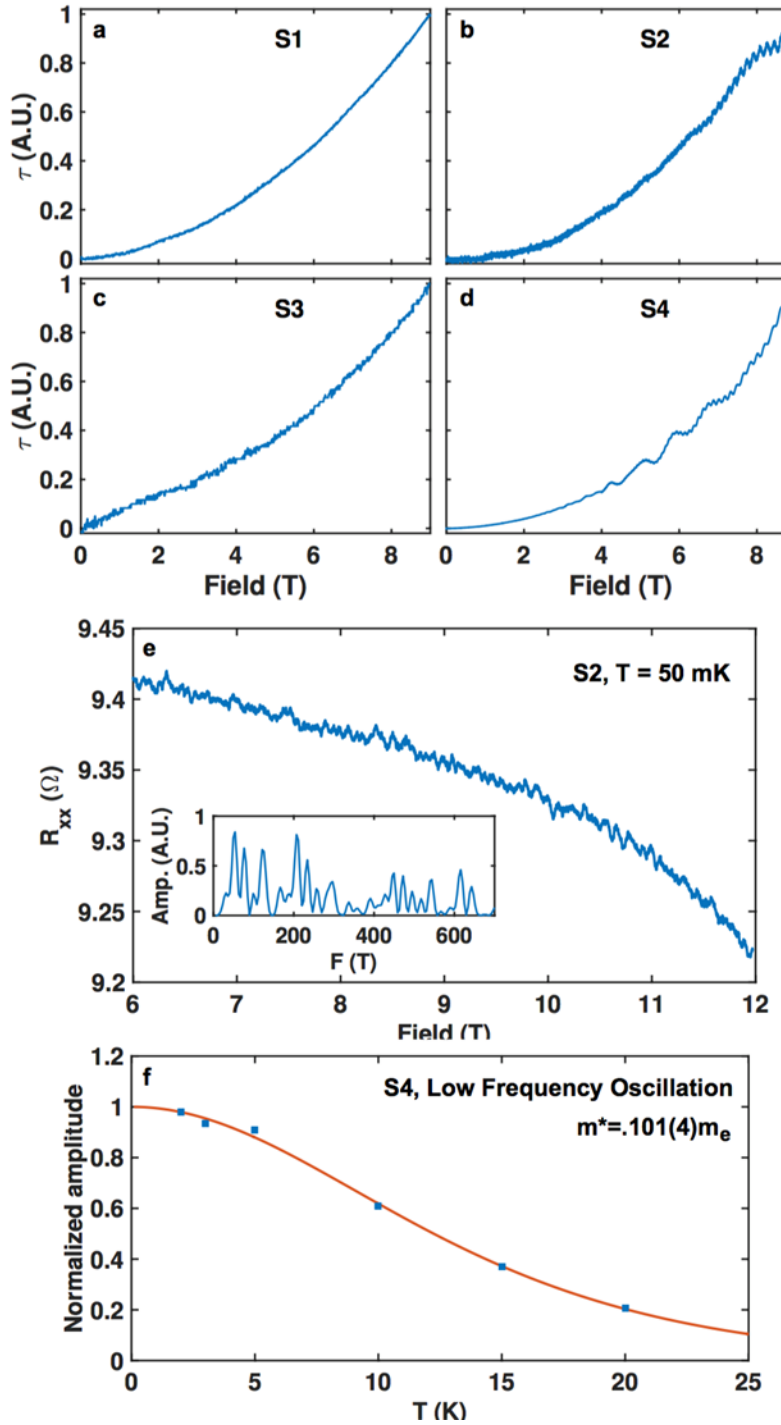


Figure 23: dHvA Quantum Oscillation of SmB₂ Crystals from 30 mK to 25 K Temperatures

Figure (a) through (d) quantum oscillations using torque magnetometry. (e) Magnetoresistance of S2 at 50 mK. Inset shows FFT of resistivity data after subtracting quadratic background. (f) Plot of the amplitude of the low frequency oscillations in S4 at 8.3 T, showing the effective mass

To check the impurity effect, we have deliberately measured one sample with known impurity (Figure 24).

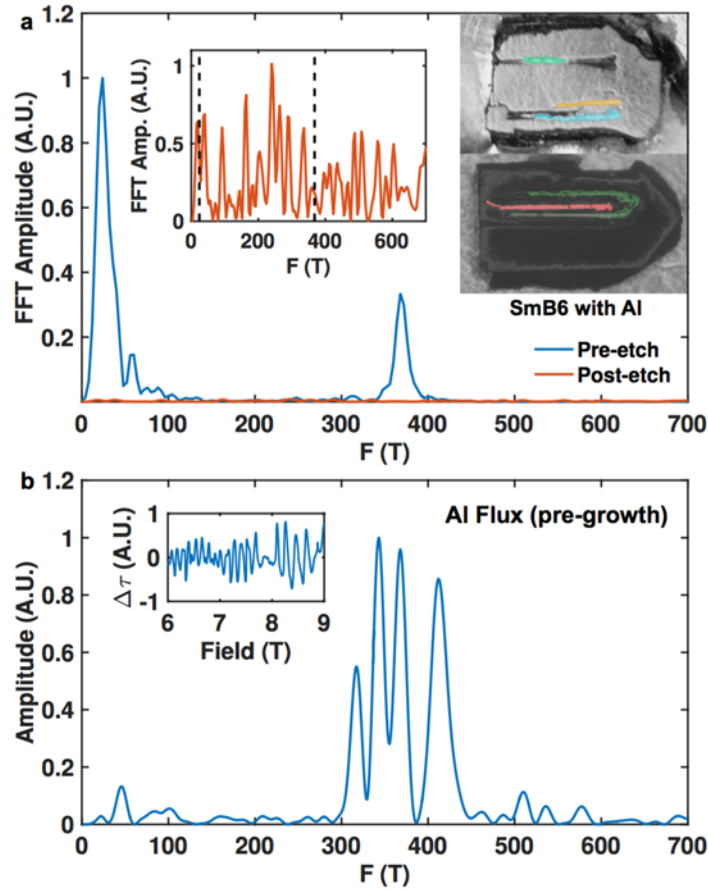


Figure 24: FFT of dHvA Data of Pure and Impure Samples

(a) *FFT of dHvA data on a SmB6 crystal containing discontinuous aluminum deposits. Left inset shows the frequency spectrum after etching away Aluminum inclusions. The right inset shows pictures of the sample after polishing. The highlighted colors indicate the aluminum deposits.* (b) *Frequency spectrum of high purity aluminum pellet used as flux in SmB6 crystal growth. The inset shows the torque signal*

One of the crystals exhibiting dHvA oscillations was polished to determine whether the oscillation were extrinsic or intrinsic in origin. As shown in the inset of Figure 24(a), three disconnected aluminum inclusions were found after polishing away the top portion of the crystal. After further polishing, two more disconnected inclusions were discovered. Surprisingly, frequency analysis showed only a couple of peaks in the frequency spectrum, despite the presence of multiple aluminum inclusions. Figure 24(b) shows dHvA oscillations from a small piece of high purity aluminum used as flux during the growth process. There are multiple peaks in the 300–400 T range due to the fact that the pellet is amorphous and composed of many randomly arranged micro-crystals. Considering there are 5 distinct aluminum inclusions in the SmB6 crystal, the lack of multiple peaks demonstrates that the inclusions are all aligned along the same crystallographic axis. The fact that embedded aluminum inclusions are arranged nearly

epitaxially with the SmB₆ was recently reported in a study combining neutron diffraction, powder diffraction, and x-ray computed tomography.

Having established the origin of the dHvA signal in SmB₆ with high impurity level, we now turn to a comparison of the angular dependence of the oscillation frequencies to that of the recent report. Figure 25 shows the angular dependence of the dHvA in a SmB₆ crystal as it rotated 90° in a (100) plane. The observed oscillation frequencies are compared with the β and γ pockets providing a near-perfect match. [11] The lack of observation of the higher frequency oscillations is due to the lower fields used in the present study. At 18 T compared to 9 T, the oscillation amplitude of the β oscillations is expected to increase by a factor of 14 (a factor of 2 from the linear scaling of the torque magnetometry signal with applied field and a factor of 7 from the Dingle damping factor). The angular dependence of the observed oscillations also agree with early reports on the dHvA oscillations of single-crystal aluminum. Comparing the angular dependence of the SmB₆ with that from aluminum shows that the [100] axis of the aluminum inclusions within SmB₆ are very nearly aligned with the SmB₆ [100] axis.

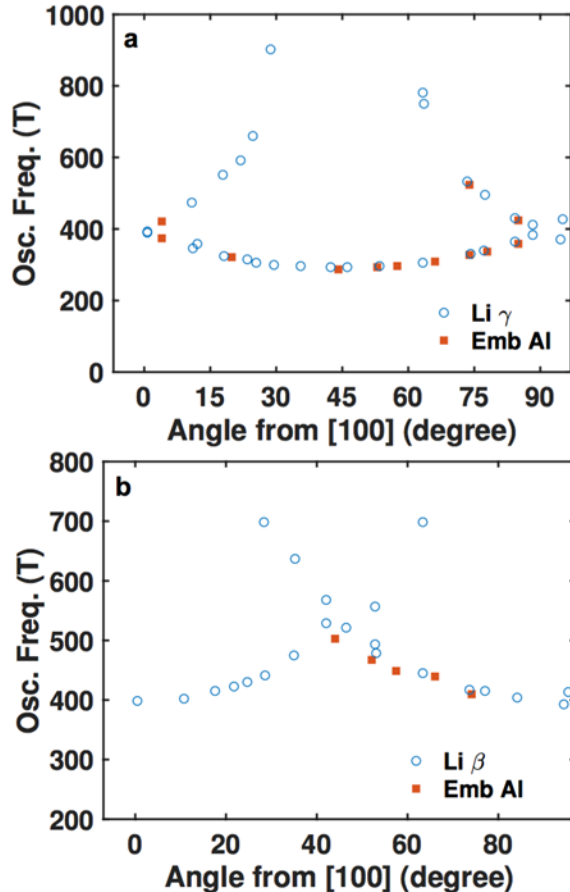


Figure 25: Angular Dependence of dHvA Data
 (a) dHvA frequency for the γ pocket and (b) Angular dependence of the dHvA oscillation frequency for the β pocket

Near 1 K, the bulk of SmB₆ is truly insulating, which explains the lack of any observation of SdH oscillations in SmB₆ or transport evidence of the superconducting transition from subsurface aluminum inclusions. Aluminum has a superconducting critical temperature of 1.17 K and a critical field of 105 Oersted. Figure 26(a) and (b) show transport measurements performed on a SmB₆ crystal near the superconducting transition of aluminum. No feature is visible in resistance plotted versus either temperature or field. Unlike transport measurements, which are incapable of probing beyond the surface, the presence of aluminum impurities can be detected through magnetic measurements capable of probing the bulk. As shown in Figure 26(c), evidence of the aluminum superconducting transition is visible AC susceptibility measurements. Above 1.2 K, no feature is observed in susceptibility. As the temperature is lowered, a feature is observed in susceptibility that tracks the critical field expected for the aluminum superconducting transition.

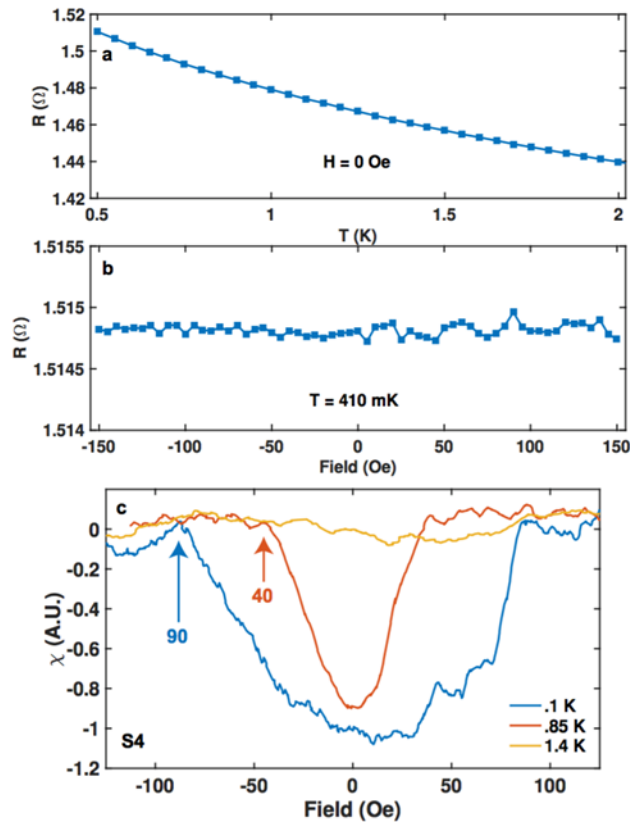


Figure 26: Resistance Measurements

(a) Resistance at zero field for a SmB₆ crystal with a subsurface aluminum inclusion. (b) Resistance versus field at 410 mK for a SmB₆ crystal with a subsurface aluminum inclusion. (c) AC Susceptibility measurement of SmB₆ crystal near zero field

Even though evidence of the aluminum inclusion is easily obtained from bulk magnetic measurements, it is not visible through transport measurements. After the transport and susceptibility measurements were performed, the sample was polished to determine the proximity of the aluminum inclusions to the surface. Subsurface aluminum deposits became visible after only several polishing laps, showing that the inclusion was separated from the

surface by less than 100 μm . Due to the high insulating bulk, an aluminum inclusion that is shallowly embedded within the bulk is completely isolated from the metallic surface state. Thus, when performing screening of SmB₆ samples for aluminum inclusions, it is not sufficient to check for impurities by only measuring transport.

In conclusion, using dHvA quantum oscillation measurements we found no evidence of significant change of the electronic structure of the surface at least up to 25 K, suggesting that the cause of the rapid reduction of dephasing length is not an intrinsic effect of the surface state of SmB₆, but instead is most likely an extrinsic effect due to magnetic impurity. Our measurement do suggest that large amount of impurity could however introduce false dHvA signals. We still need to continue working on finding a solution for removing the magnetic impurity for the TQUID magnetometer for work at reasonable temperatures.

4.0 CONCLUSIONS

In summary, in this project, we have demonstrated a RF tunable oscillator device, perhaps the first real-life device of topological Kondo insulator. We have developed a quantitative theory that matches perfectly with experimental results. As referees for our paper “Radio Frequency Tunable Oscillator Device Based on SmB6 Micro-crystal” put it:

Quote: “The paper describes a novel device based on a correlated topological insulator material SmB6. As a Kondo insulator with possible topological properties, this system generated a lot of interest, especially since in the recent years the surface states were actually observed and linked to resistivity anomaly at low temperatures. The paper builds on and supports the topological states prediction, using the coupling of surface and bulk states to produce useful dynamical behavior. The thermal and electrical coupling of surface to bulk states is used to propose, model, construct and test a novel type of an oscillator device. The device operates up to a MHz range, but further extension to THz is postulated to be possible by reducing crystal size....Very nice and enjoyable piece. I strongly recommend publication.”

Quote: “The paper describes the utilization of a SmB6 micro-crystal in a tunable oscillator device. The paper presents intriguing results, which represent, as far as I am aware, one of the first applications of the unique properties of TIs for a real life application. The experimental work presented here is technically challenging and skillfully performed.”

We have also demonstrated a TQUID magnetometer, although only working at mK extremely low temperatures due to limited dephasing length. The latter is likely due to physics that we don't yet understand.

5.0 REFERENCES

1. D. Kim, T. Grant, Z. Fisk, Limit cycle and anomalous capacitance in the Kondo insulator SmB₆. *Phys Rev Lett.* **109**, 096601 (2012).
2. D. J. Kim, J. Xia, Z. Fisk, Topological surface state in the Kondo Insulator Samarium Hexaboride. *Nat Mater.* **13**, 446–470 (2014).
3. T. L. Naing, T. O. Rocheleau, E. Alon, C.-C. Nguyen, A 78-microwatt GSM phase noise-compliant Pierce oscillator referenced to a 61-MHz wine-glass disk resonator, 562–565 (2013).
4. CRC, *The MEMS Handbook* (CRC Press, ed. 1, 2011).
5. R. M. Cerdà, *Understanding Quartz Crystals and Oscillators* (Artech House, 2014).
6. M. R. Halesh, K. R. Rasane, H. Rohini, in *link.springer.com* (Springer Berlin Heidelberg, Berlin, Heidelberg, 2011), vol. 125 of *Communications in Computer and Information Science*, pp. 472–478.
7. J. H. Bardarson, J. E. Moore, Quantum interference and Aharonov–Bohm oscillations in topological insulators. *Rep Prog Phys.* **76**, 056501 (2013).
8. B. L. Altshuler, A. A, *ELECTRON-ELECTRON INTERACTIONS IN DISORDERED CONDUCTORS* (Elsevier, New York, ed. 1, 1985).
9. J. J. Cha *et al.*, Weak Anti-localization in Bi₂(Se_xTe_{1-x})₃Nanoribbons and Nanoplates. *Nano Lett.* **12**, 1107–1111 (2012).
10. X. Wu, X. Li, Z. Song, C. Berger, W. A. de Heer, Weak Anti-localization in Epitaxial Graphene: Evidence for Chiral Electrons. *Phys Rev Lett.* **98**, 136801 (2007).
11. I. Garate, L. Glazman, Weak localization and anti-localization in topological insulator thin films with coherent bulk-surface coupling. *Phys Rev B.* **86** (2012), doi:10.1103/PhysRevB.86.035422.
12. J. J. Cha *et al.*, Effects of Magnetic Doping on Weak Anti-localization in Narrow Bi₂Se₃Nanoribbons. *Nano Lett.* **12**, 4355–4359 (2012).
13. H.-T. He *et al.*, Impurity Effect on Weak Anti-localization in the Topological Insulator Bi₂Te₃. *Phys Rev Lett.* **106**, 166805 (2011).
14. H. Peng *et al.*, Aharonov-Bohm interference in topological insulator nanoribbons. *Nat Mater.* **9**, 225–229 (2010).
15. P. Coleman, Heavy fermions: Electrons at the edge of magnetism. *Handbook of Magnetism and Advanced Magnetic Materials* (2007).
16. J. KONDO, Resistance Minimum in Dilute Magnetic Alloys. *Prog. Theor. Phys.* **32**, 37–

& (1964).

17. X.-L. Qi, S.-C. Zhang, Topological insulators and superconductors. *Rev Mod Phys.* **83**, 1057–1110 (2011).
18. M. Hasan, C. Kane, Colloquium: Topological insulators. *Rev Mod Phys.* **82**, 3045–3067 (2010).
19. S. Hikami, A. I. Larkin, Y. Nagaoka, Spin-Orbit Interaction and Magnetoresistance in the Two Dimensional Random System. *Prog. Theor. Phys.* **63**, 707–710 (1980).
20. V. Alexandrov, M. Dzero, P. Coleman, Cubic topological Kondo insulators. *Phys Rev Lett.* **111**, 226403 (2013).
21. F. Lu, J. Zhao, H. Weng, Z. Fang, X. Dai, Correlated topological insulators with mixed valence. *Phys Rev Lett.* **110**, 096401 (2013).
22. S. Wolgast *et al.*, Low-temperature surface conduction in the Kondo insulator SmB 6. *Phys Rev B.* **88**, 180405 (2013).
23. X. Zhang *et al.*, Hybridization, inter-ion correlation, and surface states in the Kondo insulator SmB6. *Phys. Rev. X.* **3**, 011011 (2013).
24. D. J. Kim *et al.*, Surface Hall Effect and Nonlocal Transport in SmB6: Evidence for Surface Conduction. *Scientific Reports.* **3** (2013), doi:10.1038/srep03150.
25. S. Thomas *et al.*, Weak anti-localization and linear magnetoresistance in the surface state of SmB. *arXiv:1307.4133* (2013).
26. M. Tian *et al.*, Dual evidence of surface Dirac states in thin cylindrical topological insulator Bi2Te3 nanowires. *Scientific Reports.* **3** (2013), doi:10.1038/srep01212.
27. S. S. Hong, Y. Zhang, J. J. Cha, X.-L. Qi, Y. Cui, One-Dimensional Helical Transport in Topological Insulator Nanowire Interferometers. *Nano Lett* (2014), doi:10.1021/nl500822g.
28. W. Pan *et al.*, Exact Quantization of the Even-Denominator Fractional Quantum Hall State at $v=5/2$ Landau Level Filling Factor. *Phys Rev Lett.* **83**, 3530–3533 (1999).
29. H. Lefèvre, *The fiber-optic gyroscope* (Artech House on Demand, ed. 1, 1993).
30. J. Xia, P. T. Beyersdorf, M. M. Fejer, A. Kapitulnik, Modified Sagnac interferometer for high-sensitivity magneto-optic measurements at cryogenic temperatures. *Appl Phys Lett.* **89** (2006), doi:10.1063/1.2336620.
31. R. Jaklevic, J. Lambe, A. Silver, J. Mercereau, Quantum Interference Effects in Josephson Tunneling. *Phys Rev Lett.* **12**, 159–160 (1964).
32. C. Kittel, *Introduction to Solid State Physics* (Wiley, 2004).

6.0 RESULTING PUBLICATIONS

Maxim Dzero, Jing Xia, Victor Galitski, Piers Coleman, “Topological Kondo Insulators”, Annual Review of Condensed Matter Physics, Volume 7 (2016).

A. Stern, D.K. Efimkin, V. Galitski, Z. Fisk and J. Xia, “Radio Frequency Tunable Oscillator Device Based on SmB₆ Micro-crystal”, Phys. Rev. Lett. 116(16), 166603, (2016).

“Weak Anti-localization and Linear Magnetoresistance in The Surface State of SmB₆” is waiting for reviewer report (2016).

LIST OF ACRONYMS AND ABBREVIATIONS

ACRONYM	DESCRIPTION
AAS	Altshuler-Aronov-Spivak
AB	Aharonov-Bohm
AC	alternating current
AC	alternating current
ARPES	angle resolved photoemission spectroscopy
DC	direct current
dHvA	De Haas-van Alphen
EDS	energy dispersive x-ray spectroscopy
FFT	Fast Fourier Transform
FWHM	full width at half maximum
HLN	Hikami-Larkin-Nagaoka
MEMS	microelectromechanical systems
MR	magnetoresistance
OHFC	oxygen free-high conductivity
PCB	printed circuit board
PPMS	Physical Property Measurement System
RF	radio frequency
RRR	residual resistance ratio
SdH	Shubnikov-de Hass
SEM	scanning electron microscope
SQUID	superconducting quantum interference device
TI	topological insulator
TKI	topological Kondo insulator
TQUID	topological quantum interference device
VCO	voltage-controlled-oscillator
WAL	weak anti-localization